Thrusting and exhumation of the southern Mongolian Plateau: joint thermochronological constraints from the Langshan Mountains, western Inner Mongolia, China

Li-Xia Feng, Roderick W. Brown, Bao-Fu Han, Zeng-Zhen Wang, Katarzyna Łuszczak, Bo Liu, Zhi-Cheng Zhang, Jian-Qing Ji

PII: S1367-9120(17)30001-9
DOI: http://dx.doi.org/10.1016/j.jseaes.2017.01.001
Reference: JAES 2919

To appear in: *Journal of Asian Earth Sciences*

Received Date: 13 May 2016
Revised Date: 3 January 2017
Accepted Date: 4 January 2017

Please cite this article as: Feng, L-X., Brown, R.W., Han, B-F., Wang, Z-Z., Łuszczak, K., Liu, B., Zhang, Z-C., Ji, J-Q., Thrusting and exhumation of the southern Mongolian Plateau: joint thermochronological constraints from the Langshan Mountains, western Inner Mongolia, China, *Journal of Asian Earth Sciences* (2017), doi: http://dx.doi.org/10.1016/j.jseaes.2017.01.001

Thrusting and exhumation of the southern Mongolian Plateau: joint thermochronological constraints from the Langshan Mountains, western Inner Mongolia, China

Li-Xia Feng[a], Roderick W. Brown[b], Bao-Fu Han[a*], Zeng-Zhen Wang[a], Katarzyna Łuszczak[b,c], Bo Liu[a], Zhi-Cheng Zhang[a], Jian-Qing Ji[a]

[a] Key Laboratory of Orogenic Belts and Crustal Evolution of Ministry of Education, School of Earth and Space Sciences, Peking University, Beijing 100871, China

[b] School of Geographical and Earth Sciences, College of Science and Engineering, University of Glasgow, Glasgow G12 8QQ, United Kingdom

[c] Scottish Universities Environmental Research Centre, East Kilbride G75 0QF, United Kingdom

Corresponding author: Bao-Fu Han

Email address: bfhan@pku.edu.cn

ABSTRACT

The Mongolian Plateau has undergone multi-stage denudation since the Late Triassic, and the NE-trending Langshan Mountains in the southern margin of the Mongolian Plateau is crucial to unraveling the Meso-Cenozoic cooling and exhumation history of the Mongolian Plateau. The Langshan Mountains are dominated by Precambrian gneiss and Permian–Middle Triassic granitic plutons crosscut by a set of NE-striking thrust faults. A joint thermochronological study was conducted on 31 granitic and gneissic samples along the HQ and CU transects across the Langshan Mountains and other two samples from the BQ in the north of the Langshan Mountains. Four biotite/muscovite and three K-feldspar $^{40}Ar/^{39}Ar$ plateau ages range from 205 ± 1 to 161 ± 1 and 167 ± 1 to 131 ± 1 Ma, respectively. Thirty three apatite fission track (AFT) ages are between 184 ± 11 and 79 ± 4 Ma, with mean track lengths from 11.1 ± 1.8 to 13.1 ± 1.4 μm of mostly unimodal distributions. Thirty one single-grain raw AHe ages are in a range of 134 ± 8 to 21 ± 1 Ma. The AFT ages decrease monotonously from NW to SE until thrust faults along the two transects, with an age-jump across thrust F35. Joint thermal history modelling shows a three-stage cooling history as a result of denudation, especially with spatial differentiation in the first stage. Relative slow cooling at c. 0.6–1.0 °C/Ma occurred in the BQ and the northern part of the HQ transect during 220–100 Ma and the northern part of the CU transect during 160–100 Ma, respectively, with an amount of c. 2–3 km denudation between 160 and 100 Ma, implying little movement along the thrusts F13 and F33. In the middle and southern parts of the HQ transect and the southern part of the CU transect, rapid cooling at c. 4.0–7.0 °C/Ma, with c. 6–9 km denudation during 170–130

or 160–100 Ma, respectively, was probably influenced by thrusting of F35, F38 and F42 and the resultant tilting. A combination of thrusting, tilting, and denudation led to the youngering trends towards thrusts in different parts. However, there was no significant denudation across the Langshan Mountains in the second stage from 100–80 Ma until the last stage of rapid denudation (c. 2 km) since 20–10 Ma, which was simultaneous with the rapid uplift of the northern part of the Tibetan Plateau at c. 15 Ma. A youngering trend of AFT ages from the inner to the peripherals of the Mongolian Plateau implies the outward propagation of the Mongolian Plateau since the Mesozoic.

Key words

The Langshan Mountains; The Mongolian Plateau; Thrust; Exhumation; Biotite/Muscovite and K-feldspar $^{40}Ar/^{39}Ar$; Apatite fission track; Apatite (U-Th)/He; Thermal history modelling.

1. Introduction

The Mongolian Plateau is within the Asain continent and has an average elevation of 2000 m above sea-level and is surrounded by the Baikal area, the Sayan Mountains, the Altay Mountains, the Gobi-Altay Mountains, the Beishan Mountains, the Langshan Mountains, the Daqingshan Mountains, the Yanshan Mountains, and the Greater Hinggan Mountains (Fig. 1). Geologically, the Mongolian Plateau comprises part of the Central Asia Orogenic Belt (CAOB) and the northern margin of the North China Craton

(NCC), and they are separated by the Chifeng-Bayan Obo Fault (Fig. 1). The CAOB is a major Phanerozoic accretionary orogen seated between the European Craton (EC) to the west, the Siberian Craton (SC) to the east, and the NCC to the south (e.g., Windley et al., 2007; Xiao et al., 2009). The accretion process of the CAOB is related to the tectonic evolution of the Paleo-Asian Ocean (e.g., Tang et al., 1990; Han et al., 2011; Xu et al., 2013) and the final closure of the Paleo-Asian Ocean resulted in the amalgamation of the NCC and CAOB during the Late Permian to Triassic (e.g., Xiao et al., 2003, Zhang et al., 2007a, 2009a, 2009b; Miao et al., 2008; Jian et al., 2010). In the CABO, the closure of the Mongol–Okhotsk orogen shows a youngering trend from the Permian–Jurassic in the west to Late Jurassic–Early Cretaceous in the east (Zonenshain et al., 1990; Cogné et al., 2005; Tomurtogoo et al., 2005).

During the Mesozoic, the Mongolian Plateau and surroundings have undergone strong intra-continental deformation (e.g., Zheng et al., 1991, 1996; Davis et al., 1998, 2001; Darby et al., 2001; Darby and Ritts, 2002; Wang et al., 2011 and references therein; Faure et al., 2012; Dong et al., 2015). The ongoing convergence of the Indian and Eurasian plates during the Cenozoic has greatly influenced much of the Asian continent from the southern Himalayan front to the northern SC (e.g., Molnar and Tapponnier, 1975; Yin and Harrison, 2000).

The Mongolian Plateau is thus an ideal place to study intra-continental deformation in Asia during the Meso-Cenozoic. The formation of the Mongolian Plateau may be related to the India–Eurasia collision (e.g., De Grave et al., 2007; Vassallo et al., 2007) or from the interaction of a mantle plume with the continental lithosphere (e.g., Windley and Allen, 1993; Huang et al., 2015). Recent studies suggest that the plateau has been tectonically uplifted since the Early and Middle Jurassic and

its current altitude has been preserved since the last tectonic event at around 8 Ma (Jolivet et al., 2007), but a large quantity of apatite fission track (AFT) data also indicate rapid uplift and erosion across the Mongolian Plateau during the Mesozoic (Fig. 1). The Mesozoic uplift of the Mongolian Plateau may be related to the Mongol–Okhotsk orogeny, the sequential collision of the Qiangtang and Lhasa blocks with Eurasia, and the subduction of the Paleo-Pacific plate, or their combined impacts (e.g., De Grave and Van den Haute, 2002; Li et al., 2011; Glorie et al., 2012).

The Langshan Mountains in the western Inner Mongolia, China, are the westernmost part of the Yinshan–Yanshan orogenic belt in the southern margin of the Mongolian Plateau (Fig. 1; Darby and Ritts, 2007; Davis et al., 2010), and thus a joint thermochronlogical study on the Langshan Mountains will provide insights into the formation and evolution of the Mongolian Plateau.

2. Geological setting

Topographically, the Langshan Mountains, with an average elevation of 1500–2000 m in most parts, gently decrease northward and northwestward, in contrast with the significant southward decreases from c. 2000 m near Huogeqi to c. 1000 m near Qingshan and Urad Houqi in the Jilantai-Hetao basin (Figs. 1 and 2).

Except for widespread distibutions of Mesozoic and Cenozoic sedimetary sequences and local outcrops of Late Paleozoic sedimentary sequences (Fig. 2; BGMRNMAR, 1991), the central part of the Langshan Mountains comprises Neoarchean to Paleoproterozoic gneiss, Meso-Neoproterozoic metasedimentary rocks, and Late Paleozoic (Fig. 2; Wu et al., 2013; Wang et al., 2015, 2016). The youngest

pluton was emplaced at 236 ± 2 Ma (zircon U-Pb age, unpublished data).

In the southeastern piedmont of the Langshan Mountains, the Mesoproterozoic basement rocks are unconformably overlain by Jurassic or Cretaceous sequences (Fig. 2; BGMRNMAR, 1991). The Jurassic sequences are >1 km in thickness and show finer upward, whereas >2.5 km thick Cretaceous strata are composed of conglomerate, sandstone, and shale. The conglomerate clasts include non-foliated granitoids, gneiss, schist, and sandstone, indicating a proximal source (Darby and Ritts, 2007).

The pre-Mesozoic rocks are crosscut by major NE-striking thrusts, which are locally transected by subordinate NEN or NWN strike-slip faults (Fig. 2). Thrust F42 in the southeastern piedmont of the Langshan Mountains occurs in the Jurassic-Lower Cretaceous sequences, but it was active during the Late Jurassic to Early Cretaceous (Darby and Ritts, 2007). In the interior of the Langshan Mountains, thrust F13 was active before the Late Cretaceous (see Fig. 2). Along thrusts F32 and F33, a Triassic pluton (zircon U-Pb age of 241 ± 1 Ma; unpublished data) and its older country rocks were thrusted over the Lower Cretaceous sequences (Fig. 2). Both of the thrusts F35 and F38 crosscut the granitic plutons with a zircon U-Pb age of 236 ± 2 Ma (unpublished data). Therefore, thrusts F42, F32, F33, F35, and F38 may have been active since the Triassic, except for the pre-Late Cretaceous thrust F13. In addition, a Pliocene-Quaternary active mountain-front normal fault, as part of the Ordos graben system (Zhang et al., 1998), separates the Langshan Mountains from the Jilantai-Hetao Basin (Fig. 2), in which more than 10 km thick fluvio-lacustrine clastic sediments have been deposited during the Cenozoic (SSBC, 1988).

3. Sampling and analytical procedures

3.1. Sampling

Thirty one samples were collected along two transects across the Langshan Mountains and major thrusts, and other two samples were from the Bayin Qiandamen (BQ) area in the north of the Langshan Mountains (Figs. 2 and 3; Table 1).

The HQ transect from Huogeqi to Qingshan traverses the most rugged part of the Langshan Mountains (Fig. 2), and can be divided by thrusts F33, F35, and F38 into northern, middle, and southern parts (Figs. 3 and 5a). Eighteen granitic samples with zircon U-Pb ages from 297 ± 2 to 236 ± 2 Ma (unpublished data) were collected between 1227 and 2102 m (ASL) and performed for AFT analysis. Therein, two samples CG13-11 and CG13-15 were also used for biotite and K-feldspar $^{40}Ar/^{39}Ar$ dating and four samples 10LS-03, 10LS-17, CG13-13, and CG13-15 for apatite (U-Th)/He (AHe) analysis (Fig. 3a; Table 1).

Along the CU transect from Chaoge Ondor to Urad Houqi (Fig. 2), seven granitic samples with zircon U-Pb ages from 269 ± 2 to 241 ± 1 Ma (unpublished data) and six Precambrian granitic gneiss samples were collected between 1112 and 1839 m (ASL). All samples were used for AFT analysis. Therein, one sample CG13-02 was selected for biotite and K-feldspar $^{40}Ar/^{39}Ar$ dating and another sample CG12-20 for muscovite and K-feldspar $^{40}Ar/^{39}Ar$ dating (Table 1). The current watershed is located between samples CG12-14 and CG12-28 and the CU transect is divided into northern and southern parts (Figs. 3a and 5b).

In addition, two granitic samples, with a zircon U-Pb age of 262 ± 3 Ma

(unpublished data), were collected at 1517 and 1519 m (ASL) in the BQ, northern part of the Langshan Mountains, where the topography is relatively flat (Fig. 2). Only AFT analysis was conducted on both samples (Table 1).

3.2. Analytical procedures

Biotite, muscovite, K-feldspar, and apatite grains were separated using the standard procedures, including crushing, sieving and heavy liquid and magnetic separation methods. Biotite/Muscovite and K-feldspar $^{40}Ar/^{39}Ar$ and AFT analyses were conducted in the Key Laboratory of Orogenic Belts and Crustal Evolution, at Peking University. AHe analysis was prepared at Fission Track Lab in the University of Glasgow and measured in the Scottish Universities Environmental Research Centre (SUERC), respectively. Individual techniques are described in detail in the Supplementary Text 1.

Each sample is modelled individually using QTQt software (Gallagher, 2012) in order to extract its thermal history. The modelling space is randomly sampled using the Markov Chain Monte Carlo (MCMC) algorithm. The multi-compositional annealing model with c-axis projected length (Ketcham et al., 2007a, 2007b) is adopted for fission track annealing. The initial mean track length is all determined using the mean Dpar value of each sample with the formula suggested by Carlson et al. (1999). For the samples which also have AHe data, all single-grain raw AHe ages are jointly inverted using the radiation damage accumulation and annealing model of Gautheron et al. (2009). If necessary, a set of samples from different elevations is modelled together (joint modelling) to represent a quasi-vertical profile, because the joint modelling can

average out the complex deviations of individual samples, and the resultant thermal histories may simultaneously fit all samples from the vertical profile (Gallagher, 2012).

For individual modelling, the modelling space is simply constrained by the sample fission track age ± sample fission track age on time and 70 ± 70 °C on temperature. The present-day temperature is set to 10 ± 10 °C. Whenever possible, additionally independent geological constraints are added to improve modelling results. Individual modelling of samples CG13-11, CG13-15, and CG12-20 is constrained by their biotite/muscovite and K-feldspar $^{40}Ar/^{39}Ar$ data and the zircon U-Pb age of the youngest pluton (236 ± 2 Ma). The MCMC is run for at least 100,000 iterations for post-burn-in and burn-in, respectively.

For joint modelling of vertical profiles, an additional model parameter, i.e., present-day temperature offset between the top and bottom sample, should be taken into account. The present-day surface heat flow in the Langshan Mountains is estimated to be 40–60 mW/m (Lysak, 2009), similar to those in the surroundings of the Langshan Mountains (Hu et al., 2001), and thus the Langshan Mountains may also have the same present geothermal gradient of 20 to 30 °C/km as those in the nearby area (Hu et al., 2001). Therefore, a large range of possible geothermal gradient value of 25 ± 25 °C/km is used to calculate the present-day temperature offset. Joint modelling all starts from the latest magmatic activity (236 ± 2 Ma) and, if applicable, is constrained by biotite/muscovite and K-feldspar $^{40}Ar/^{39}Ar$ cooling ages. The MCMC is run at least 200,000 iterations for burn-in and 800,000 iterations for post-burn-in in order to better deal with a larger number of the input data and a higher complexity of the models.

The output of QTQt modelling is a collation of all thermal history models with

associated posterior probabilities. The expected model, which is adopted here, retains well constrained and robust features and averages out more complex T-t deviations observed in only a small number of possible models. More details about thermal history modelling approaches using QTQt can be found in Wildman et al. (2015).

4. Results

4.1. Biotite/muscovite and K-feldspar $^{40}Ar/^{39}Ar$ ages

Two samples from the HQ transect and one sample from the CU transect were performed for biotite and K-feldspar $^{40}Ar/^{39}Ar$ dating, and one sample from the CU transect was used for muscovite and K-feldspar $^{40}Ar/^{39}Ar$ dating (Table 1). The biotite/muscovite and K-feldspar $^{40}Ar/^{39}Ar$ data (Supplementary Text 2 and Supplementary Table 1) all show a disturbed age spectrum (Fig. 4). Except for K-feldspar separates from one sample (CG13-02), the other biotite/muscovite and K-feldspar separates all yielded $^{40}Ar/^{39}Ar$ plateau ages (Fig. 4). Four biotite/muscovite $^{40}Ar/^{39}Ar$ plateau ages range from 205 ± 1 to 161 ± 1 Ma (Fig. 4), and three K-feldspar $^{40}Ar/^{39}Ar$ plateau ages vary from 167 ± 1 to 148 ± 1 Ma (Fig. 4). Seven $^{40}Ar/^{39}Ar$ plateau ages are generally consistent with their corresponding isochron ages.

4.2. AFT

AFT ages of 33 samples all passed the χ^2 test (P (χ^2) > 5%) and all the measured grains in each sample show similar annealing kinetic properties (Dpar values) (e.g.,

O'Sullivan and Parrish, 1995; Carlson et al., 1999; Ketcham et al., 2007b). AFT ages of single grains in each sample are thus classified as one population and expressed by the AFT central ages (Green, 1981).

4.2.1. The HQ transect

In the HQ transect, eighteen AFT ages range from 184 ± 11 to 85 ± 7 Ma (Fig. 5a; Table 2) and are significantly younger than the emplacement age of the youngest pluton (236 ± 2 Ma). In the northern part to the northwest of thrust F33, four AFT ages of 184 ± 11 to 164 ± 11 Ma display a youngering trend towards northwest and show no sharp age-jumps across thrust F13 (Fig. 5a; Table 2). In the middle part between thrusts F33 and F35, nine AFT ages vary from 158 ± 19 to 91 ± 7 Ma and decrease monotonously towards southeast until an age-jump across thrust F35 (Fig. 5a; Table 2). In the southern part between thrusts F35 and F38, the other five AFT ages of 114 ± 5 to 85 ± 7 Ma again decrease towards southeast until thrust F38 (Fig. 5a; Table 2).

Along this transect, seventeen samples have similar Dpar values of 1.4–1.9 μm, except for sample 10LS-3 with a longer Dpar value of 3.2 μm (Table 2). The mean track lengths (MTLs) are in ranges of 11.6 ± 1.9 to 13.1 ± 1.4 μm in three samples of the northern part, 11.1 ± 1.8 to 12.7 ± 1.8 μm in nine samples of the middle part, and 11.8 ± 1.6 to 12.4 ± 1.4 μm in three samples of the southern part (Table 2). Track length distributions of each sample display unimodal and negatively skewed patterns (Figs. 7–9, SF1, and SF2).

4.2.2. The CU transect

Thirteen samples from the CU transect yielded AFT ages of 147 ± 11 to 79 ± 4 Ma (Fig. 5b; Table 2). Similarly, AFT ages show a youngering trend from 147 ± 11 to 92 ± 8 Ma in the northern part and from 118 ± 7 to 79 ± 4 Ma in the southern part until thrust 42 as elevations decrease, but the four samples from a quasi-vertical profile show increasing AFT ages of 108 ± 5 to 116 ± 5 Ma with lowering elevations (Fig. 5b; Table 2).

All the samples, however, have similar Dpar values of 1.2–1.6 μm (Table 2), and their track length distributions are negatively skewed and unimodal, with the MTLs varying from 12.4 ± 1.4 to 12.7 ± 1.3 μm (Figs. 10, 11, SF3, and SF4; Table 2).

4.2.3. The BQ

Twenty one and 26 countable apatite grains in samples CG12-01 and CG12-02 from the BQ yielded AFT ages of 147 ± 8 and 136 ± 7 Ma, respectively (Fig. 5c). The two samples have identical Dpar values of 1.2 μm and their track length distributions are unimodal, with the MTLs of 12.4 ± 1.4 and 11.9 ± 1.5 μm, respectively (Fig. 13; Table 2).

4.3. AHe

AHe analysis was performed only on four samples from the HQ transect (Table 3), and their raw single-grain AHe ages are in ranges of 134 ± 8 to 87 ± 5 Ma for

sample 10LS-03, 112 ± 7 to 29 ± 2 Ma for sample CG13-13, 113 ± 7 to 63 ± 4 Ma for sample CG13-15, and 60 ± 4 to 21 ± 1 Ma for sample 10LS-17.

Raw single-grain AHe ages from one single sample have large degrees of dispersion, ranging from 43 to 130% (Table 3). Samples 10LS-3 and CG13-15 show a positive correlation between raw single-grain AHe ages and crystal width (Figs. 6a and 6e), but samples CG13-13 and 10LS-17 show no clear correlations (Figs. 6c and 6g). Furthermore, the AHe ages and (eU) content in all four samples show no linear relationship (Figs. 6b–6h).

4.4. Summary of joint thermochronological data

It is clear that the ages obtained from different minerals are consistent well with their closure temperatures (Table 4), suggesting the sequential cooling of the dated minerals. Most of the AFT samples show a positive correlation between ages and elevations (Fig. 5), but the four samples from the quasi-vertical profile in the southern part of the CU transect display an inverted age-elevation trend (Fig. 5b). Such an abnormal age-elevation relationship is probably due to rapid stream trenching other than faulting, just like that of the glacial erosion in the Namche Barwa Peak, eastern Himalayan syntaxis (Tu et al., 2015). However, these four AFT ages are compatible with others along the southern part of the CU transect. Therefore, all of the $^{40}Ar/^{39}Ar$, AFT, and AHe data can be used for thermal history modelling.

5. Thermal history modelling results

Out of 33 AFT samples, 25 samples have sufficient confined fission tracks (46–188) for individual modelling, but all the 33 samples were treated as three vertical profiles in the northern, middle, and southern parts of the HQ transect and two profiles in the northern and southern parts of the CU transect in order to perform joint modelling. Results from joint modelling and representative individual modelling are displayed in Figs. 7–12, and the other individual modelling results can be found in Figs. SF1–SF4.

5.1. The HQ transect

After the emplacement of the Middle Triassic granitic pluton, the thermal history of the northern part of the HQ transect may be divided into three stages (Fig. 7): (1) rapid cooling from c. 115 to c. 25 °C during c. 220 and c. 100 Ma (c. 0.75 °C/Ma); (2) little cooling between c. 100 and c. 15 Ma, and (3) relatively rapid cooling from c. 40 °C to the current surface temperature after c. 15 Ma (c. 2.0 °C/Ma).

The thermal history of the middle part of the HQ transect, after cooling of the pluton to the closure temperature of c. 250 °C for K-feldspar $^{40}Ar/^{39}Ar$ age, may be divided into three stages (Fig. 8): (1) rapid cooling from 250 to 75–50 °C between c. 170 and 130 Ma (c. 4–5 °C/Ma and subsequently slow cooling from 85–60 to 40–20 °C during 120 and 80 Ma (c. 1.0 °C/Ma), (2) little cooling until c. 10 Ma, and (3) relatively rapid cooling from 65–40 °C to the current surface temperature after c. 10 Ma (c. 3.0–5.5 °C/Ma).

Similarly, the southern part of the HQ transect is also characterized by three cooling stages (Fig. 9): (1) rapid cooling from c. 350 to c. 70–80 °C during 170 and 130

Ma (c. 7.0 °C/Ma) and subsequently slow cooling from 90–80 to 35–25 °C between 120 and 80 Ma (1.4 °C/Ma), (2) little cooling until c. 10 Ma, and (3) relatively rapid cooling from 55–45 °C to the current surface temperature after c. 10 Ma (c. 3.5–4.5 °C/Ma).

5.2. The CU transect

In the northern part of the CU transect, the thermal history was also divided into three stages after the emplacement of the Middle Triassic granitic pluton (Fig. 10): (1) slow cooling from c. 120 to c. 60 °C during 160–100 Ma (c. 1.0 °C/Ma); (2) little cooling until c. 12 Ma; and (3) relatively rapid cooling from 50–40 °C to the current surface temperature since c. 12 Ma (c. 2.5–3.3 °C/Ma).

The southern part of this transect also revealed a three-stage thermal history after the cooling of the pluton to the closure temperature of c. 325 °C for muscovite $^{40}Ar/^{39}Ar$ age (Fig. 11): (1) rapid cooling from c. 325 °C to c. 50 °C between 160 and 100 Ma (c. 4.6 °C/Ma); (2) little cooling until c. 15 Ma; and (3) relatively rapid cooling from 55–45 °C to the current surface temperature since c. 15 Ma (c. 2.3–3.0 °C/Ma).

5.3. The BQ

The BQ is also featured by three stages of cooling following the emplacement of the Middle Triassic granitic pluton (Fig. 12): (1) slow cooling from c. 100 to c. 40 °C between c. 200 and c. 100 Ma (c. 0.6 °C/Ma); (2) little cooling between c. 100 and c. 20 Ma, and (3) relatively rapid cooling from c. 40 °C to the current surface temperature

after c. 20 Ma (c. 1.5 °C/Ma).

5.4. Assessment of the modelling qualities

Predicted AFT data of all samples from thermal history modelling are within 80% of the observed values, except for two samples (CG12-18 and CG12-20; Figs. 7c, 8c, 9c, 10c, 11c, and 12; see Figs. SF1–SF44 for more individual modelling predictions). However, the predicted AHe ages of about half dated grains are within 80% of the measured ages (Figs. 7c, 8c, 9c, 10c, and 11c; see Figs. SF1–SF4 for more individual modelling predictions). Wildman et al. (2016) explained the poor fit of the AHe data relative to that of AFT data.

6. Discussion

The joint thermal history modelling revealed that the Langshan Mountains has experienced three-stage cooling since the Late Triassic, which may be outlined as follows: (1) contrasting cooling in different parts before c. 100–80 Ma, (2) little cooling between c. 100–80 and c. 20–10 Ma, and (3) rapid cooling from 65–40 °C to the present-day surface temperature since c. 15 Ma (c. 1.5–5.5 °C/Ma). In particular, the last two stages of cooling have been recorded throughout the whole Langshan Mountains.

6.1. Exhumation of the Langshan Mountains

For the first stage of cooling, the BQ and the northern parts of the HQ and CU transects show similar cooling at c. 0.6–1.0 °C/Ma, in contrast to that in the middle and southern parts of the HQ transect and in the southern part of the CU transect. The first stage in the southern part of the CU transect is characterized by rapid cooling (at c. 4.6 °C/Ma) during 160–100 Ma only (Fig. 11), whareas two sub-stages are identified in the middle and southern parts of the HQ transect: early rapid cooling (c. 4.0–7.0 °C/Ma) during 170–130 Ma and following slow cooling (c. 1.0–1.4 °C/Ma) during 120–80 Ma (Figs. 8 and 9).

It is estimated that the first-stage cooling started at c. 220 Ma, which was postponed to the youngest plutonism at 236 Ma, so that the cooling revealed by joint thermal history modelling has resulted mainly from denudation. The amount of denudation in each stage can be calculated assuming two geothermal gradients of 30 and 20 °C/km for rapid and slow denudation, respectively, because rapid denudation will enhance the geothermal gradient (e.g., Braun, 2002). Consequently, the BQ and the northern parts of the HQ and CU transects underwent denudation of c. 2–3 km (160–100 Ma), significantly lower than denudation of c. 6–9 (170–130 Ma) plus c. 2–3 (120–80 Ma) km in the middle and southern parts of the HQ transect and c. 9 km (160–100 Ma) in the southern part of the CU transect (Fig. 3a). If the current average geothermal gradient is 25 °C/km, an amount of denudation c. 1.2–2.2 km is estimated for the last stage since c. 15 Ma.

The denudation of c. 6–9 km in the interior part of the Langshan Mountains during 170–100 Ma is partially recorded by the >3.5 km thick Jurassic to Early Cretaceous clastic sequences in the southeastern piedmont of the Langshan Mountains (Fig. 2), in which the conglomerate clasts include Precambrian basement rocks and

granitic rocks, suggesting a local source for the sediments (Darby and Ritts, 2007).

6.2. Impacts of thrusting on denudation of the Langshan Mountains

It is known that five major thrusts develop in the Langshan Mountains, especially in the area transversed by the HQ transect (Figs. 2 and 3), and those thrusts would have affected the Meso-Cenozoic denudation of the Langshan Mountains. Although cooling of rocks does not directly arise from thrusting (e.g., Platt, 1993), the variations of AFT data in a cross-section may be related to thrust faulting in the case of sufficiently rapid erosion (e.g., Lock and Willett, 2008). Thrusting first uplifts rocks on the hanging wall. The materials above the erosional surface would be removed and underlying rocks would cool down, which may be recorded by different thermochronological systems. The thrusting may result in the tilting of thrust sheets and exposure of deeper rocks so that the magnitude of uplift and denudation become larger towards thrusts (e.g., ter Voorde et al., 2004; Lock and Willett, 2008; Metcalf et al., 2009), accompanied by a younger trend of AFT ages (see Figs. 5 and 13). Similar cases occur also in the Bogeda Mountain of the Chinese Tian Shan (Tang et al., 2015) and the Longmenshan in the eastern margin of the Tibetan Plateau (Tan, 2012). In the present case, the youngering trend of AFT ages towards thrusts and large denudation of c. 6–9 km in the middle and southern parts of the HQ transect and the southern part of the CU transect might have been related to thrusting.

Detailedly, the four AFT ages from both sides of thrust F13 show a consistently decreasing trend with elevations, without a sharp age-jump across thrust F13 (Figs. 5a and 14a), implying that the thrusting was little when it was active before the Late

Cretaceous (Fig. 2), and thus the hanging and foot walls show slow cooling (c. 0.6–1.0 °C/Ma) during 220–100 Ma, with similar denudation of c. 2 km on both sides of thrust F13 from 160 to 100 Ma (Figs. 3a and 7). Similarly, there are no age-jumps across thrust F33 (Figs. 5a and 14a), suggesting that thrust F33 had little contribution to denudation of the middle part from 170 to 130 Ma (Figs. 3a and 8). However, the middle and southern parts show a monotonous decrease in AFT ages southeastward until the northwest-dipping thrusts F35 and F38 (Figs. 5a and 14a), with an age-jump across thrust F35 and larger denudation of c. 9 km in the southern part than that (c. 6–7 km) in the middle part during 170–130 Ma (Figs. 3a and 9). Generally, the decreasing AFT ages and increasing denudation from north to south should be controlled by F35 and F38 thrusting and the resultant tilting of the thrust sheets (Fig. 3b).

In addition to the similar patterns of AFT ages with elevations along the HQ and CU transects, both transcets also show comparable denudation in the first stage (see Fig. 3 for details), but the patterns of AFT ages with elevations and denudation in the southern part of the CU transect may have been controlled only by thrust F42.

Apparently, thrusts F35, F38, and F42 have had important impacts on the denudation of the Langshan Mountains during 170–100 Ma. This is in agreement with the contractional period in the whole Yinshan–Yanshan orogenic belt during the Middle Jurassic to Early Cretaceous (e.g., Zhang et al., 2007b; Lin et al., 2013).

6.3. Implications for the Mongolian Plateau

In the Langshan Mountains, the rapid cooling and denudation occurred mainly before 100–80 Ma. The AFT data available from the literature clearly show that the

Late Triassic to Cretaceous AFT ages have been reported from most parts of the Mongolian Plateau (Fig. 1 and references therein) and adjacent areas, such as the Kyrgyz Northern Tien Shan (Degrave et al., 2013), the central Chinese Tian Shan (Jolivet et al., 2010), and the northern part of the Tibetan Plateau (Jolivet et al., 2001). It is very interesting to note that the Cretaceous and younger AFT ages are principally confined to the peripherals of the plateau, such as the Baikal area, the Sayan Mountains, the Altay Mountains, the Beishan Mountains, the Langshan Mountains, the Daqingshan Mountains, the Yanshan Mountains, and the Greater Hinggan Mountains, with a youngering trend outward (Fig. 1). This implies that the outward growth of the Mongolian Plateau has occurred since the Mesozoic.

Temporally, the Mesozoic uplift and denudation of the Mongolian Plateau might be generally simultaneous with the docking of the Qiangtang and Lhasa blocks to the southern margin of Eurasian continent during the Late Triassic to Early Cretaceous (e.g., Pullen et al., 2008; Yin and Harrison, 2000), and the scissor-like closure of the Mongol–Okhotsk Ocean from west to east from Permian–Jurassic to the Early Cretaceous (e.g., Zonenshain et al., 1990; Cogné et al., 2005; Tomurtogoo et al., 2005), and the subduction of the Paleo-Pacific plate during the Early Jurassic–Cretaceous (e.g., Maruyama, 1997; Zhou et al., 2006). However, the latest uplift of the Langshan Mountains since c. 15 Ma is coeval with the exhumation of the Elashan Mountains at c. 15 Ma (Duvall et al., 2013) in the northern Tibetan Plateau and the Liupanshan Mountains at c. 8 Ma (Zheng et al., 2006) and Helanshan Mountains at c. 12 Ma (Liu et al., 2010) around the northeastern Tibetan Plateau, probably due to the distant effect of rapid uplift in the northern part of the Tibetan Plateau at c. 15 Ma (Lu et al., 2016).

7. Conclusions

Multiple thermochronological methods were applied to the samples from the HQ and CU transects and the BQ of the Langshan Mountains. Four biotite/muscovite $^{40}Ar/^{39}Ar$ plateau ages range from 205 ± 1 to 161 ± 1 Ma, three K-feldspar $^{40}Ar/^{39}Ar$ plateau ages vary between 167 ± 1 and 131 ± 1 Ma, 33 AFT ages range from 184 ± 4 to 79 ± 11 Ma, and 31 single-grain raw AHe ages range between 134 ± 8 to 21 ± 1 Ma.

Thermal history modelling using joint thermochrnological data indicates a three-stage cooling history in the Langshan Mountains: (1) rapid cooling with spatial differentiation in different parts at distinct rates before 100–80 Ma, (2) little cooling in the whole Langshan Mountains between 100–80 and 20–10 Ma, and (3) rapid cooling (c. 1.5–5.5 °C/Ma) to the present-day surface temperature also in the whole Langshan Mountains since c. 15 Ma. In the first stage, cooling at c. 0.6–1.0 °C/Ma was recorded in the northern parts of the HQ and CU transects and the BQ from 220–200 or 160 to 100 Ma, where an amount of denudation was c. 2–3 km during 160–100 Ma. In the middle-southern parts of the HQ transect and the southern part of the CU transect, the AFT ages become younger towards thrusts F35, F38, and F42, and rapid cooling (c. 4.0–7.0 °C/Ma) and remarkable denudation of c. 6–9 km from 170–130 or 160–100 Ma were probably controlled by the thrusting and the thrust-sheet tilting of F35, F38 and F42, respectively. The final stage, with the denudation of <2 km, is coeval with the rapid uplift of the northern part of the Tibetan Plateau at c. 15 Ma. Moreover, the AFT ages throughout the Mongolian Plateau show a youngering trend from the inner to the peripherals, suggesting the outward propagation of the Mongolian Plateau since the Mesozoic.

Acknowledgements

We would like to thank Mark Wildman (University of Glasgow) for double check of apatite grains and Zhongpeng Han (Edingburgh University, a visitor from China University of Geosciences Beijing) for (U-Th)/He analysis. We appreciate Professor Fin Stuart (Scottish Universities Environmental Research Centre) for his advice for AHe data and thermal history modelling. We are also grateful to two anonymous reviewers for their comments and suggestions. This work was financially supported by the Ministry of Science and Technology of China (Grant No. 2013CB429806).

References

Baksi, A.K., Archibald, D.A., Farrar, E., 1996. Intercalibration of 40Ar/39Ar dating standards. Chemical Geology 129, 307–324.

Braun, J., 2002. Quantifying the effect of recent relief changes on age-elevation relationships. Earth and Planetary Science Letters 200, 331–343.

Brown, R.W., Beaucher, R., Roper, S., Persano, C., Stuart, S., Fitzgerald, P., 2013. Natural age dispersion arising from the analysis of broken crystals. Part I: Theoretical basis and implications for the apatite (U–Th)/He thermochronometer. Geochimica et Cosmochimica Acta 122, 478–497.

Bureau of Geology and Mineral Resources of Nei Mongol Autonomous Region, 1991. Regional Geology of Nei Mongol (Inner Mongolia) Autonomous Region. In: Geological Memoirs, Series 1, No. 25. Geological Publishing House, Beijing (in

Chinese with English abstract).

Carlson, W.D., Donelick, R.A., Ketcham, R.A., 1999. Variability of apatite fission-track annealing kinetics: I. Experimental results. American Mineralogist 84, 1213–1223.

Cogné, J.P., Kravchinsky, V.A., Halim, N., Hankard, F., 2005. Late Jurassic–Early Cretaceous closure of the Mongol–Okhotsk Ocean demonstrated by new Mesozoic paleomagnetic results from the Trans-Baikal area (SE Siberia). Geophysical Journal International 163, 813–832.

Darby, B.J., Davis, G.A., Zheng, Y.D., 2001. Structural evolution of the southwestern Daqing Shan, Yinshan belt, Inner Mongolia, China. Geological Society of America Memoirs 194, 199–214.

Darby, B.J., Ritts, B.D., 2002. Mesozoic contractional deformation in the middle of the Asian tectonic collage: the intraplate Western Ordos fold thrust belt, China. Earth and Planetary Science Letters 205, 13–24.

Darby, B.J., Ritts, B.D., 2007. Mesozoic structural architecture of the Lang Shan, North-Central China: Intraplate contraction, extension, and synorogenic sedimentation. Journal of Structural Geology 29, 2006–2016.

Davis, G.A., Wang, C., Zheng, Y., Zhang, J., Zhang, C., Gehrels, G.E., 1998. The enigmatic Yinshan fold-and-thrust belt of northern China: new views on its intraplate contractional styles. Geology 26, 43–46.

Davis, G.A., Zheng, Y.D., Wang, C., Darby, B.J., Zhang, C.H., Gehrels, G., 2001. Mesozoic tectonic evolution of the Yanshan fold and thrust belt, with emphasis on Hebei and Liaoning provinces, northern China. Geological Society of America Memoirs 194, 171–197.

Davis, G.A., Darby, B.J., 2010. Early Cretaceous overprinting of the Mesozoic Daqing Shan fold-and-thrust belt by the Hohhot metamorphic core complex, Inner Mongolia, China. Geoscience Frontiers 17, 1–20.

De Grave, J., Van den haute, P., 2002. Denudation and cooling of the Lake Teleskoye Region in the Altai Mountains (South Siberia) as revealed by apatite fission-track thermochronology. Tectonophysics 349, 145–159.

De Grave, J., Buslov, M.M., Van den haute, P., 2007. Distant effects of India-Eurasia convergence and Mesozoic intracontinental deformation in Central Asia: Constraints from apatite fission-track thermochronology. Journal of Asian Earth Sciences 29, 188–204.

De Grave, J., Glorie, S., Zhimulev, F.I., Buslov, M.M., Elburg, M., Vanhaecke, F., Van den haute, P., 2011. Emplacement and exhumation of the Kuznetsk-Alatau basement (Siberia): implications for the tectonic evolution of the Central Asian Orogenic Belt and sediment supply to the Kuznetsk, Minusa and West Siberian Basins. Terra Nova 23, 248–256.

De Grave, J., Glorie, S., Buslov, M.M., Stockli, D.F., McWilliams, M.O., Batalev, V., Van den haute, P., 2013. Thermo-tectonic history of the Issyk-Kul basement (Kyrgyz Northern Tien Shan, Central Asia). Gondwana Research 23, 998–1020.

De Grave, J., Pelsmaeker, E.D., Zhimulev, F.I., Glorie, S., Buslov, M.M., Van den haute, P., 2014. Meso-Cenozoic building of the northern Central Asian Orogenic Belt: Thermotectonic history of the Tuva region. Tectonophysics 621, 44–59.

Dong, S.W., Zhang, Y.Q., Zhang, F.Q., Cui, J.J., Chen, X.H., Zhang, S.H., Miao, L.C., Li, J.H., Shi, W., Li, Z.H., Huang, S.Q., Li, H.L., 2015. Late Jurassic–Early Cretaceous continental convergence and intracontinental orogenesis in East Asia:

A synthesis of the Yanshan Revolution. Journal of Asian Earth Sciences 114, 750–770.

Dunkl, I., 2002. TRACKKEY: a Windows program for calculation and graphical presentation of fission track data. Computers & Geosciences 28, 3–12.

Duvall, A.R., Clark, M.K., Kirby, E., Farley, K.A., Craddock, W.H., Li, C.Y., Yuan, D.Y., 2013. Low-temperature thermochronometry along theKunlun andHaiyuan Faults, NE Tibetan Plateau: Evidence for kinematic change during late-stage orogenesis. TECTONICS 32, 1190–1211.

Faure, M., Lin,W., Chen, Y., 2012. Is the Jurassic (Yanshanian) intraplate tectonics of North China due to westward indentation of the North China block? Terra Nova 24 (6), 456–466.

Foeken, J., Stuart, F., Dobson, K., Persano, C., Vilbert, D., 2006. A diode laser system for heating minerals for (U-Th)/He chronometry. Geochemistry, Geophysics, Geosystems 7, 1–9.

Gallagher, K., 2012. Transdimensional inverse thermal history modeling for quantitative thermochronology. Journal of Geophysical Research 117, B02408.

Gautheron, C., Tassan-Got, L., Barbarand, J., Pagel, M., 2009. Effect of alpha-damage annealing on apatite (U–Th)/He thermochronology. Chemical Geology 266(3), 157–170, doi:10.1016/j.chemgeo.2009.06.001.

Gillespie, J., Glorie, S., Xiao, W.J., Zhang, Z.Y., Collins, A.S., Evans, N., McInnes, B., De Grave, J., 2015. Mesozoic reactivation of the Beishan, southern Central Asian Orogenic Belt: Insights from low-temperature thermochronology, Gondwana Research, http://dx.doi.org/10.1016/j.gr.2015.10.004.

Gleadow, A.J.W., Duddy, I.R., Green, P.F., Lovering, J.F., 1986. Confined fission track

lengths in apatite: a diagnostic tool for thermal history analysis. Contributions to Mineralogy and Petrology 94, 405–415.

Glorie, S., De Grave, J., Buslov, M.M., Zhimulev, F.I., Elburg, M.A., Van den haute, P., 2012. Structural control on Meso-Cenozoic tectonic reactivation and denudation in the Siberian Altai: Insights from multi-method thermochronometry. Tectonophysics 544–545, 75–92.

Green, P.F., 1981. Anew look at statistics in fission track dating. Nuclear Tracks and Radiation Measurements 9 (5), 77–86.

Hames, W.E., Bowring, S.A., 1994. An empirical evaluation of the argon diffusion geometry in muscovite. Earth and Planetary Science Letters 124, 161–169.

Han, B.F., He, G.Q., Wang, X.C., Guo, Z.j., 2011. Late Carboniferous collision between the Tarim and Kazakhstan-Yili terranes in the western segment of the South Tian Shan Orogen, Central Asia, and implications for the Northern Xinjiang, western China. Earth-Science Reviews 109 (3–4), 74–93.

Hu, S.B., He, L.J., Wang, J., 2001. Compilation of heat flow data in the China continental area (3rd edition). Chinese Journal of Geophysics 44 (5), 611–626.

Huang, F., He, L.j., Wu, Q.J., 2015. The geothermal regime and geodynamic mechanisms of the Mongolia-Baikal rift zone. Chinese Journal of Geology 50(1), 63–73.

Hurford, A.J., Green, P.F., 1983. The zeta-age calibration of fission-track dating. Isotope Geoscience 1, 285–317.

Jian, P., Liu, D.Y., Kröner, A., Windley, B.F., Shi, Y.R., Zhang, W., Zhang, F.Q., Miao, L.C., Zhang, L.Q., Tomurhuu, D., 2010. Evolution of a Permian intraoceanic arc-trench system in the Solonker suture zone, Central Asian Orogenic Belt, China

and Mongolia. Lithos 118, 169–190.

Jolivet, M., Brunel, M., Seward, D., Xu, Z., Yang, J., Roger, F., Topponnier, P., Malavieille, J., Arnaud, N., Wu, C., 2001. Mesozoic and Cenozoic tectonics of the northern edge of the Tibetan plateau: fission-track constraints. Tectonophysics 343, 111–134.

Jolivet, M., Ritz, J.F., Vassallo, R., Larroque, C., Braucher, R., Todhileg, M., Chauvet, A., Sue, C., Arnaud, N., Vicente, R.D., Arzhanikova, A., Arzhanikov, S., 2007. Mongolian summits: An uplifted, flat, old but still preserved erosion surface. Geology 35(10), 871–874.

Jolivet, M., Dominguez, S., Charreau, J., Chen, Y., Li, Y., Wang, Q., 2010. Mesozoic and Cenozoic tectonic history of the central Chinese Tian Shan: reactivated tectonic structures and active deformation. Tectonics 29, TC6019.Ketcham, R.A., Donelick, R.A., Donelick, M.B., 2000. AFTSolve: A program for multi-kinetic modeling of apatite fission-track data. American Mineralogist 2, 1–32.

Ketcham, R.A., Carter, A., Donelick, R.A., Barbarand, J., Hurford, A.J., 2007a. Improved measurement of fission-track annealing in apatite using c-axis projection. American Mineralogist 92, 789–798.

Ketcham, R.A., Carter, A., Donelick, R.A., Barbarand, J., Hurford, A.J., 2007b. Improved modeling of fission-track annealing in apatite. American Mineralogist 92, 799–810.

Li, J.F., Tang, W.H., Liu, Z., Zhang, Z.C., 2010. Apatite fission track analysis of Upper Jurassic Houcheng Formation at Qianjiadian area, Beijing and its geological significance (in Chinese with English abstract). Chinese Journal of Geophysics 53, 2907–2917.

Li, K., Jolivet, M., Zhang, Z.C., Li, J.F., Tang, W.H., 2016. Long-term Exhumation history of the Inner Mongolian Plateau constrained by apatite fission track analysis. Tectonophysics 666, 121-133.

Li, X.M., Yang, X.Y., Xia, B., Gong, G.L., Shan, Y.H., Zeng, Q.S., Li, W., Sun, W.D., 2011. Exhumation of the Dahinggan Mountains, NE China from the Late Mesozoic to the Cenozoic: New evidence from fission-track thermochronology. Journal of Asian Earth Sciences 42, 123-133.

Lin, W., Charles, N., Chen, Y., Chen, K., Faure, M., Wu, L., Wang, F., Li, Q.L., Wang, J., Wang, Q.C., 2013. Late Mesozoic compressional to extensional tectonics in the Yiwulüshan massif, NE China and their bearing on the Yinshan–Yanshan orogenic belt, Part II: Anisotropy of magnetic susceptibility and gravity modeling. Gondwana Research 23, 78–94.

Liu, J.H., Zhang, P.Z., Zheng, D.W., Wan, J.L., Wang, W.T., Du, P., Lei, Q.Y., 2010. Pattern and timing of late Cenozoic rapid exhumation and uplift of the Helan Mountain, China. Science China: Earth Science 40 (1), 50–60, doi: 10.1007/s11430-010-0016-0.

Lock, J., Willett, S., 2008. Low-temperature thermochronometric ages in fold-and-thrust belts. Tectonophysics 456 (3–4), 147–162.

Lovera, O.M., Richter, F.M., Harrison, T.M., 1989. The 40Ar/39Ar thermochronometry for slowly cooled samples having a distribution of diffusion domain sizes. Journal of Geophysical Research 94 (B12), 17917–17935.

Lu, H.J., Fu, B.H., Shi, P.L., Ma, Y.X., Li, H.B., 2016. Constraints on the uplift mechanism of northern Tibet. Earth and Planetary Science Letters 453, 108–118.

Ludwig, K.P., 2003. User's Manual for Isoplot 3.0: A geochronological toolkit for

Microsoft Excel, vol. 4. Berkeley Geochronological Center, Special Publication, 1–71.

Lysak, S.K., 2009. Thermal history, geodynamics, and current thermal activity of lithosphere in China. Russian Geology and Geophysics 50, 815–825.

Maruyama, S., 1997. Pacific-type orogeny revisited: Miyashiro-type orogeny proposed. Island Arc 6, 91–120.

McDougall, I., Harrison, T.M., 1999. Geochronology and Thermochronology by the 40Ar/39Ar Method. Oxford University Press, New York.

McDowell, F.W., McIntosh, W.C., Farley, K.A., 2005. A precise 40Ar/39Ar reference age for the Durango apatite (U-Th)/He and fission-track dating standard. Chemical Geology 214, 249–263.

Metcalf, J.R., Fitzgerald, P.G., Baldwin, S.L., Muñoz, J. A., 2009. Thermochronology of a convergent orogen: Constraints on the timing of thrust faulting and subsequent exhumation of the Maladeta Pluton in the Central Pyrenean Axial Zone. Earth and Planetary Science Letters 287, 488–503.

Miao, L.C., Fan,W.M., Liu, D.Y., Zhang, F.Q., Shi, Y.R., Guo, F., 2008. Geochronology and geochemistry of the Hegenshan ophiolitic complex: implications for late-stage tectonic evolution of the Inner Mongolia–Daxinganling Orogenic Belt, China. Journal of Asian Earth Sciences 32 (5), 348–370.

Molnar, P., Tapponnier, P., 1975. Cenozoic tectonics of Asia: effects of a continental collision. Science 189 (4201), 419–426.

Naeser, C.W., Cebula, G.T., 1985. Re-collection of fish canyon tuff for fission-track standardization. Nuclear Tracks and Radiation Measurements 10, 393.

O'Sullivan, P.B., Parrish, R.R., 1995. The importance of apatite composition and

single-grain ages when interpreting fission track data from plutonic rocks: a case study from the Coast Ranges, British Columbia. Earth and Planetary Science Letters 132, 213–224.

Platt, J.P., 1993. Exhumation of high-pressure rocks: a review of concepts and processes. Terra Nova 5 (2), 119–133.

Pullen, A., Kapp, P., Gehrels, G.E., Vervoort, J.D., Ding, L., 2008. Continental subduction in central Tibet Mediterranean-style closure of the Paleo-Tethys Ocean. Geology 36, 351–354.Sobel, E.R., Seward, D., 2010. Influence of etching conditions on fission-track etch pit diameter. Chemical Geology 271, 59–69.

State Seismology Bureau, 1988. Peripheral active fault system around the Ordos (in Chinese). Seismological Press, Beijing.

Staudacher, Th., Jessberger, E.K., Dörflinger, D., Kiko, J., 1978. A refined ultrahigh-vacuum furnace for rare gas analysis. Journal of Physics E Scientific Instruments 11, 781–784. http://dx.doi.org/10.1088/0022-3735/11/8/019.

Steiger, R.H., Jäger, E., 1977. Subcommission on geochronology: convention on the use of decay constants in geo-and cosmochronology. Earth and Planetary Science Letters 36, 359–362. http://dx.doi.org/10.1016/0012-821X(77)90060-7.

Tan, X.B., 2012. Cenozoic thermal history of the Longmenshan thrust belt: implication for the uplift mechanism in the eastern margin of the Tibetan plateau [Doctor]. Institute of Geology, China Earthquake Administration (in Chinese with English abstract).

Tang, K.D., 1990. Tectonic development of Paleozoic foldbelts at the north margin of the Sino–Korean craton. Tectonics 9 (2), 249–260.

Tang, W.H., Zhang, Z.C., Li, J.F., Li, K., Luo, Z.W., Chen, Y., 2015. Mesozoic and

Cenozoic uplift and exhumation of the Bogda Mountain, NW China: Evidence from apatite fission track analysis. Geoscience Frontiers 6, 617–625.

ter Voorde, M., de Bruijne, C.H., Cloetingh, S.A.P.L., Andriessen, P.A.M., 2004. Thermal consequences of thrust faulting: simultaneous versus successive fault activation and exhumation. Earth and Planetary Science Letters 223, 395–413.

Tomurtogoo, O., Windley, B.F., Kröner, A., Badarch, G., Liu, D.Y., 2005. Zircon age and occurrence of the Adaatsag ophiolite and Muron shear zone, central Mongolia: constraints on the evolution of the Mongol–Okhotsk ocean, suture and orogen. Journal of the Geological Society London 162, 125–134.

Tu, J.Y., Ji, J.Q., Sun, D.X., Gong, J.F., Zhong, D.L., Han, B.F., 2015. Thermal structure, rock exhumation, and glacial erosion of the Namche Barwa Peak, constraints from thermochronological data. Journal of Asian Earth Sciences 105, 223–233.

Van der Beek, P.A., Delvaux, D., Andriessen, P.A.M., Levi, K.G., 1996. Early Cretaceous denudation related to convergent tectonics in the Baikal region, SE Siberia. Journal of the Geological Society 153, 515–523.

Vassallo, R., Jolivet, M., Ritz, J.F., Braucher, R., Larroque, C., Sue, C., Todbileg, M., Javkhlanbold, D., 2007. Uplift age and rates of the Gurvan Bogd system (Gobi-Altay) by apatite fission track analysis. Earth and Planetary Science Letters 259, 333–346.

Wang, T., Zheng, Y.D., Zhang, J.J., Zeng, L.S., Donskaya, T., Guo, L., Li, J.B., 2011. Pattern and kinematic polarity of late Mesozoic extension in continental NE Asia: Perspectives from metamorphic core complexes. Tectonics 30, TC6007.

Wang, Z.Z., Han, B.F., Feng, L.X., Liu, B., 2015. Geochronology, geochemistry and origins of the Paleozoic–Triassic plutons in the Langshan area, western Inner

Mongolia, China. Journal of Asian Earth Sciences 97, 337–351.

Wang, Z.Z., Han, B.F., Feng, L.X., Liu, B., Zheng, B., Kong, L.J., 2016. Tectonic attribution of the Langshan area in western Inner Mongolia and implications for the Neoarchean–Paleoproterozoic evolution of the Western North China Craton: Evidence from LA-ICP-MS zircon U–Pb dating of the Langshan basement. Lithos, http://dx.doi.org/10.1016/j.lithos.2016.03.005.

Wildman, M., Brown, R., Watkins, R., Carter, A., Gleadow, A., Summerfield, M., 2015. Post break-up tectonic inversion across the southwestern cape of South Africa: New insights from apatite and zircon fission track thermochronology. Tectonophysics 654, 30–55.

Wildman, M., Brown, R., Beucher, R., Persano, C., Stuart, F., Gallepher, K., Schwanethal, J., Carter, A., 2016. The chronology and tectonic style of landscape evolution along the elevated Atlantic continental margin of South Africa resolved by joint apatite fission track and (U-Th-Sm)/He thermochronology. Tectonics 35, 511–545. doi:10.1002/2015TC004042.

Windley, B.F., Allen, M.B., 1993. Mongolian plateau: Evidence for a late Cenozoic mantle plume under central Asia. Geology 21(4), 295–298.

Windley, B.F., Alexeiev, D., Xiao, W.J., Kröner, A., Badarch, G., 2007. Tectonics models for accretion of the Central Asian Orogenic Belt. Journal of the Geological Society, London 164, 31–47.

Wolf, R.A., Farley, K.A., Silver, L.T., 1996. Helium diffusion and low temperature thermochronometry of apatite. Geochimica et Cosmochimica Acta 60, 4231–4240.

Wu, Y.F., Zeng, J.N., Cao, J.J., Wu, Z.Q., Chen, J.H., Zhou, S.D., Lu, S.F., Li, X.F.,

2013. Zircon U–Pb ages and Hf isotopes of Hercynian intrusion in Dongshengmiao, Inner Mongolia. Geological Science and Technology Information 32, 22–30 (in Chinese with English abstract).

Wu, Z.H., Cui, S.Q., Wu G.G., Zhu, D.G., Feng, X.Y., Ma, Y.S., 2000. Thermochronological Analysis on the Uplift Process of the Yanshan Mountains. Geological Review 46, 49–57.

Wu, Z.H., Wu, Z.H, 2003. Uplift history of the Daqing Mountain since the Late Cretaceous. ACTA GEOSCIENTIA SINICA 24 (3), 205–210.

Xiao, W.J., Windley, B.F., Hao, J., Zhai, M.G., 2003. Accretion leading to collision and the Permian Solonker suture, Inner Mongolia, China: termination of the Central Asian orogenic belt. Tectonics 22 (6), 1069.

Xiao,W.J.,Windley, B.F., Huang, B.C., Han, C.M., Yuan, C., Chen, H.L., Sun,M., Sun, S., Li, J.L., 2009. End-Permian to mid-Triassic termination of the accretionary processes of the southern Altaids: implications for the geodynamic evolution, Phanerozoic continental growth, and metallogeny of Central Asia. International Journal of Earth Sciences 98 (6), 1189–1217.

Xu, B., Charvet, J., Chen, Y., Zhao, P., Shi, G.Z., 2013. Middle Paleozoic convergent orogenic belts in western Inner Mongolia (China): framework, kinematics, geochronology and implications for tectonic evolution of the Central Asian Orogenic Belt. Gondwana Research 23, 1342–1364.

Yin, A., Harrison, T.M., 2000. Geological evolution of the Himalayan Tibetan orogen. Annual Review in Earth and Planetary Sciences 28, 211–280.

Yuan, W.M., Carter, A., Dong, J.Q., Bao, Z.K., An, Y.C., Guo, Z.J., 2006. Mesozoic-Tertiary exhumation history of the Altai Mountains, northern Xinjiang,

China: New constrains from apatite fission track data. Tectonophysics 412, 183–193.

Zhang, S.H., Zhao, Y., Song, B., Yang, Z.Y., Hu, J.M., Wu, H., 2007a. Carboniferous granitic plutons from the northern margin of the North China block: implications for a late Paleozoic active continental margin. Journal of the Geological Society 164, 451–463.

Zhang, S.H., Zhao, Y., Song, B., Hu, J.M., Liu, S.W., Yang, H.Y., Chen, F.K., Liu, X.M., Liu, J., 2009a. Contrasting Late Carboniferous and Late Permian-Middle Triassic intrusive suites from the northern margin of the North China craton: geochronology, petrogenesis, and tectonic implications. Geological Society of America Bulletin 121, 181–200.

Zhang, S.H., Zhao, Y., Kroner, A., Liu, X.M., Xie, L.W., Chen, F.K., 2009b. Early Permain plutons from the northern North China Block: constraints on continental arc evolution and convergent margin magmatism related to the Central Asian Orogenic Belt. International Journal of Earth Sciences 98, 1441–1467.

Zhang, Y.Q., Mercier, J.L., Verge´ly, P., 1998. Extension in the graben systems around the Ordos (China), and its contribution to the extrusion tectonics of south China with respect to Gobi-Mongolia. Tectonophysics 285, 41–75.

Zhang, Y.Q., Dong, S.W., Zhao, Y., Zhang, T., 2007b. Jurassic Tectonics of North China: a Synthetic View (in Chinese). Acta Geologica Sinca 81, 1462–1480.

Zheng, D.W., Zhang, P.Z., Wan, J.L., Yuan, D.Y., Li, C.Y., Yin, G.M., Zhang, G.L., Wang, Z.C., Min, W., Chen, J., 2006. Rapid exhumation at ~8 Ma on the Liupan Shan thrust fault from apatite fission-track thermochronology: Implications for growth of the northeastern Tibetan Plateau margin. Earth and Planetary Science

Letters 248, 198–208.

Zheng, Y. D., Wang, S., Wang, Y., 1991. An enormous thrust nappe and extensional metamorphic core complex newly discovered in the Sino-Mongolian boundary area. Science in China (Series D) 34, 1146–1152.

Zheng, Y., Zhang, Q., Wang, Y., Liu, R., Wang, S.G., Zuo, G., Wang, S.Z., Lkaasuren, B., Badarch, G., Badamgarav, Z., 1996. Great Jurassic thrust sheets in Beishan (North Mountains)–Gobi areas of China and southern Mongolia. Journal of Structural Geology 18 (9), 1111–1126.

Zhou, X., Sun, T., Shen, W., Shu, L., Niu, Y., 2006. Petrogenesis of Mesozoic granitoids and volcanic rocks in South China: a response to tectonic evolution. Episodes 29, 26–33.

Zonenshain, L.P., Kuzmin, M.I., Natapov, L.M., 1990. Geology of the USSR: A Plate Tectonic Synthesis, Geodyn. Ser., vol. 21, edited by L. P. Zonenshain et al., AGU, Washington, D. C.

Figure captions

Fig. 1. Simplified tectonic map of the Mongolian Plateau (after Zhang et al. 1998; Vassallo et al., 2007; Wang et al., 2011; Li et al., 2016; AFT ages from Van de Beek et al., 1996; Wu et al., 2000; De Grave and Van den Haute, 2002; Wu and Wu, 2003; Yuan et al., 2006; De Grave et al., 2007, 2011, 2014; Jolivet et al., 2007; Vassallo et al., 2007; Liu et al., 2010; Li et al., 2011, 2016; Glorie et al., 2012; Gillespie et al., 2015).

Fig. 2. Simplified geological map of the Langshan Mountains (after BGMRNMAR, 1991; Zhang et al. 1998). Numbers in boxes show zircon U-Pb ages.

Fig. 3. (a) Samples with the thermochronological ages along the HQ and CU transects (after BGMRNMAR, 1991). Rapidly denudated parts are shown in gray. (b) Schematic cross-section of the HQ transect (after Darby and Ritts, 2007) showing the impacts of thrusts on denudation of the Langshan Mountains in the first stage.

Fig. 4. Biotite/muscovite and K-feldspar $^{40}Ar/^{39}Ar$ plateau ages of four samples from the HQ and CU transects. Solid boxes were used for the plateau ages calculation.

Fig. 5. Simplified geological cross-sections of the HQ and CU transects and the BQ with thermochronological ages. See Figs. 2 and 3a for symbols.

Fig. 6. Relationship between single-grain raw AHe ages and grain width as well as the effective uranium (eU).

Fig. 7. Thermal history modelling in the northern part of the HQ transect. Black vertical lines show the cooling events interpreted. (a) T-t paths from joint modelling. (b) Zoom of the red box in figure a. (c) Relationship of AFT parameters and AHe ages versus elevations. (d) T-t paths from representative individual modelling. The color map indicates the probability distribution of tested models at a resolution of one Myr. (e) Observed track length distribution together with the measurements and predictions of the AFT and AHe parameters.

Fig. 8. Thermal history modelling in the middle part of the HQ transect. (a) T-t paths from joint modelling. (b) Zoom of the red box in figure a. (c) Relationship of AFT parameters and AHe ages versus elevations. (d) T-t paths from representative individual modelling. (e) Zoom of the red box in figure d. (f) Observed track length distribution together with the measurements and predictions of AFT and AHe parameters. See Fig. 7 for symbols.

Fig. 9. Thermal history modelling in the southern part of the HQ transect. (a) T-t paths from joint modelling. (b) Zoom of the red box in figure a. (c) Relationship of AFT parameters and AHe ages versus elevations. (d) T-t paths from representative individual modelling. (e) Zoom of the red box in figure d. (f) Observed track length distribution together with the measurements and predictions of AFT and AHe parameters. See Fig. 7 for symbols.

Fig. 10. Thermal history modelling in the northern part of the CU transect. (a) T-t

paths from joint modelling. (b) Zoom of the red box in figure a. (c) Relationship of AFT parameters versus elevations. (d) T-t paths from representative individual modelling. (e) Observed track length distribution together with the measurements and predictions of AFT parameters. See Fig. 7 for symbols.

Fig. 11. Thermal history modelling in the southern part of the CU transect. (a) T-t paths from joint modelling. (b) Zoom of the red box in figure a. (c) Relationship of AFT parameters versus elevations. (d) T-t paths from representative individual modelling. (e) Zoom of the red box in figure d. (f) Observed track length distribution together with the measurements and predictions of AFT parameters. See Fig. 7 for symbols.

Fig. 12. Individual thermal history modelling in the BQ. See Fig. 7 for symbols.

Fig. 13. Thrusting, tilting and exhumation pathways through the biotite/muscovite, K-feldspar, and AHe closure temperatures and AFT PAZ. Particularly, AFT ages of samples A, B, and C, which come from the un-annealed, partially annealed, and fully annealed zones, respectively, show a youngering trend towards the thrust. Black fine lines are references and black thick line indicates listric thrust fault. Tc: closure temperature.

Fig. 14. AFT age-elevation relationship in the HQ (a) and CU transects (b).

Table 1. Sample details and methods used in this study.

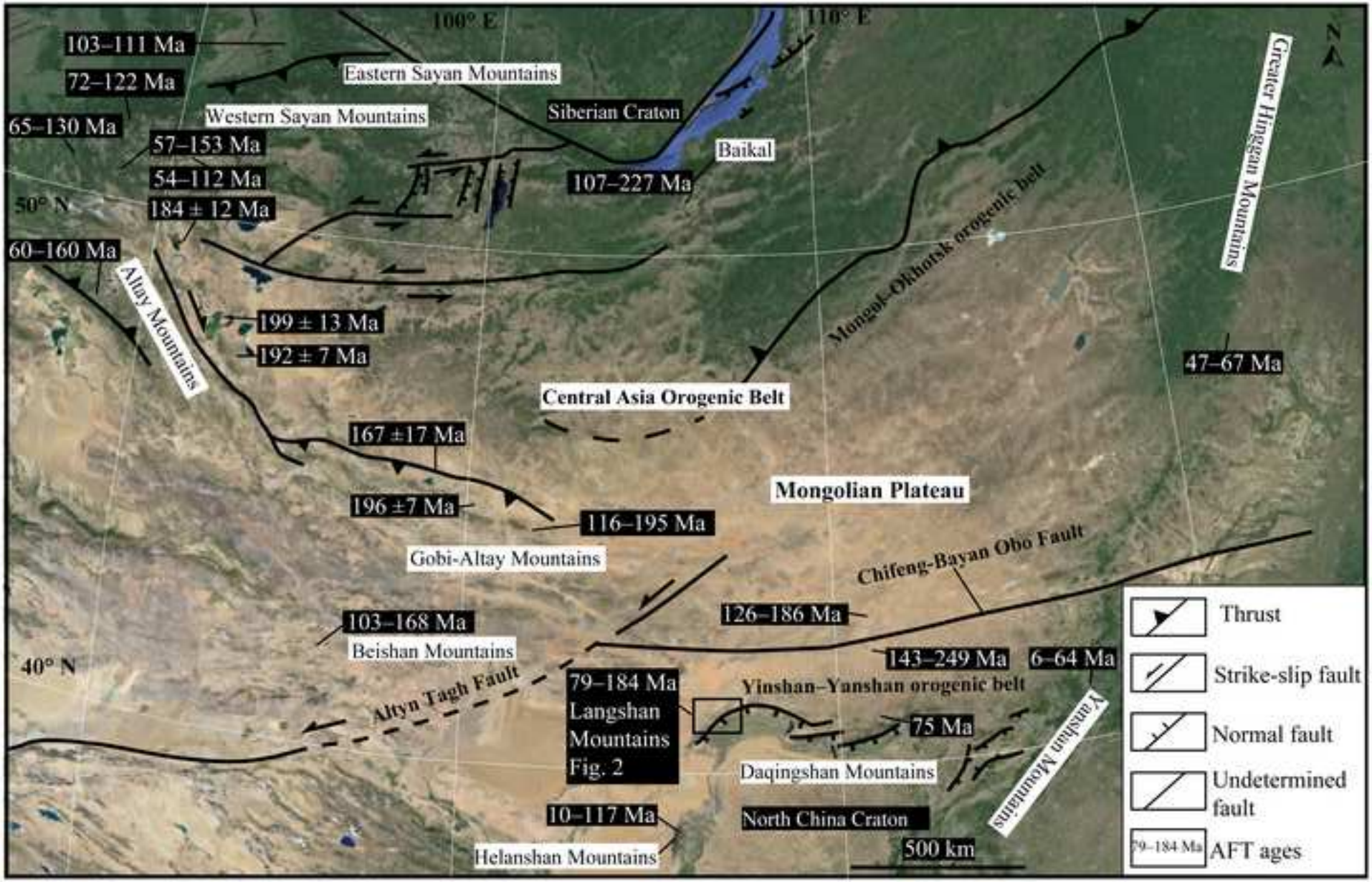

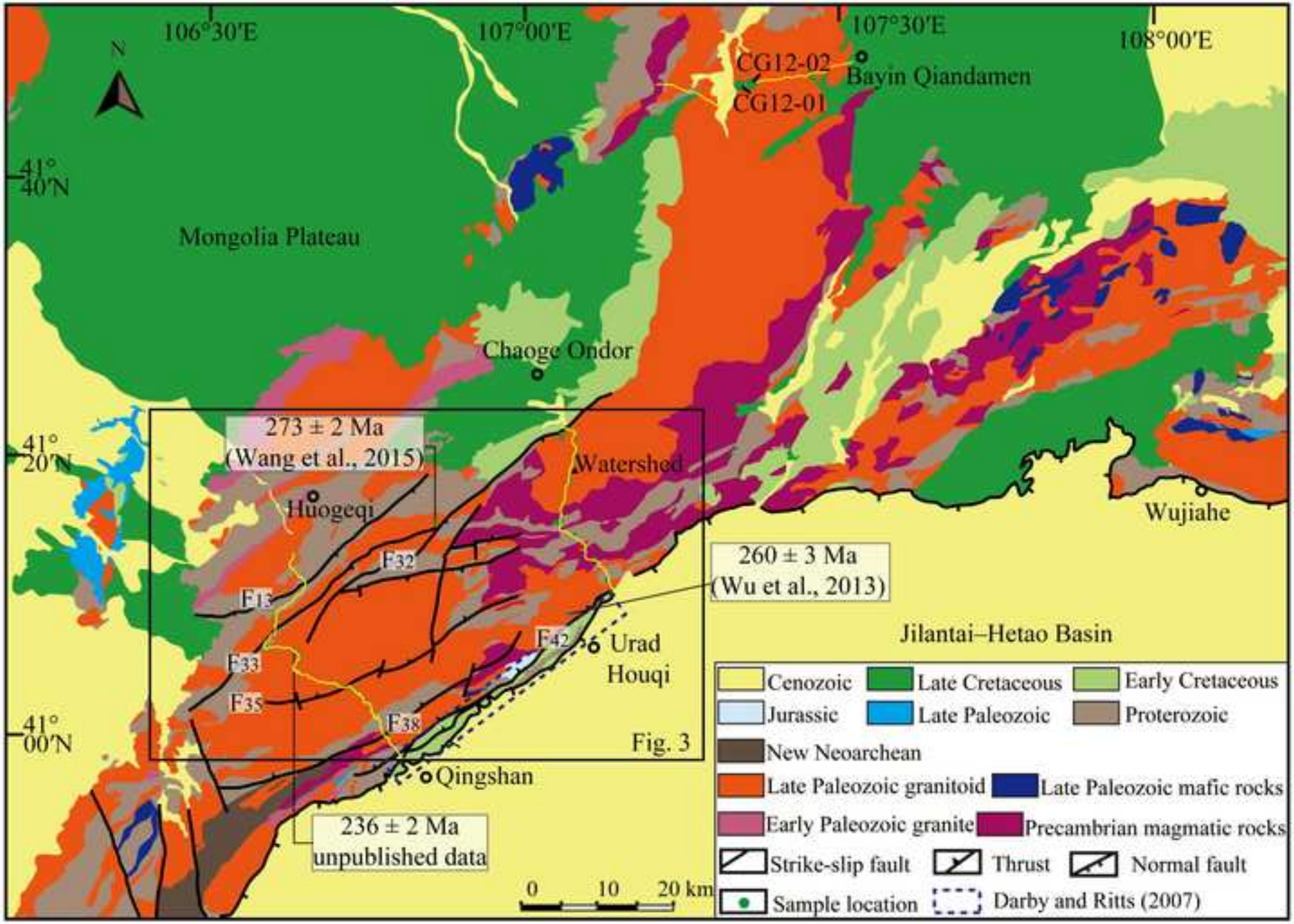

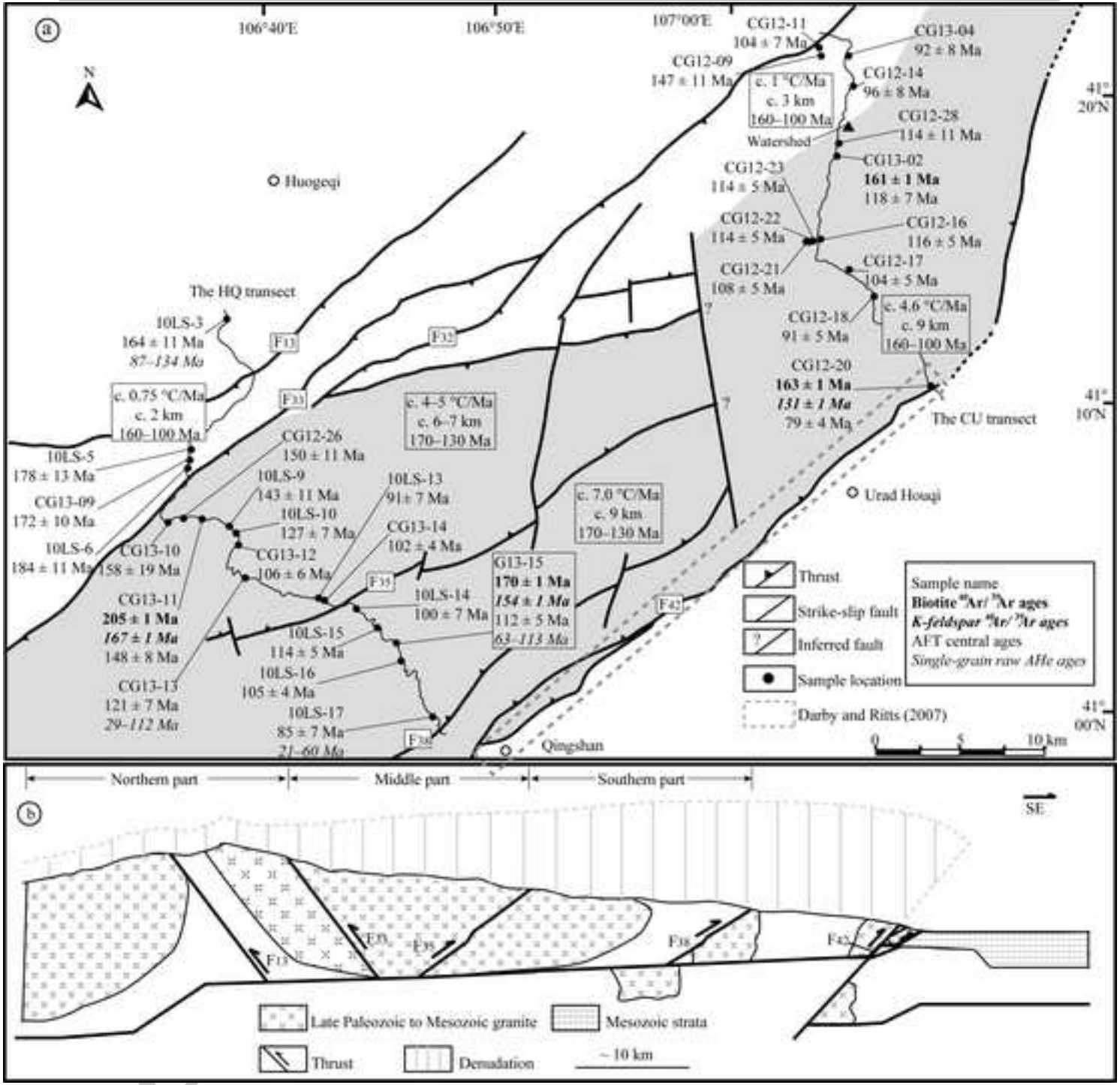

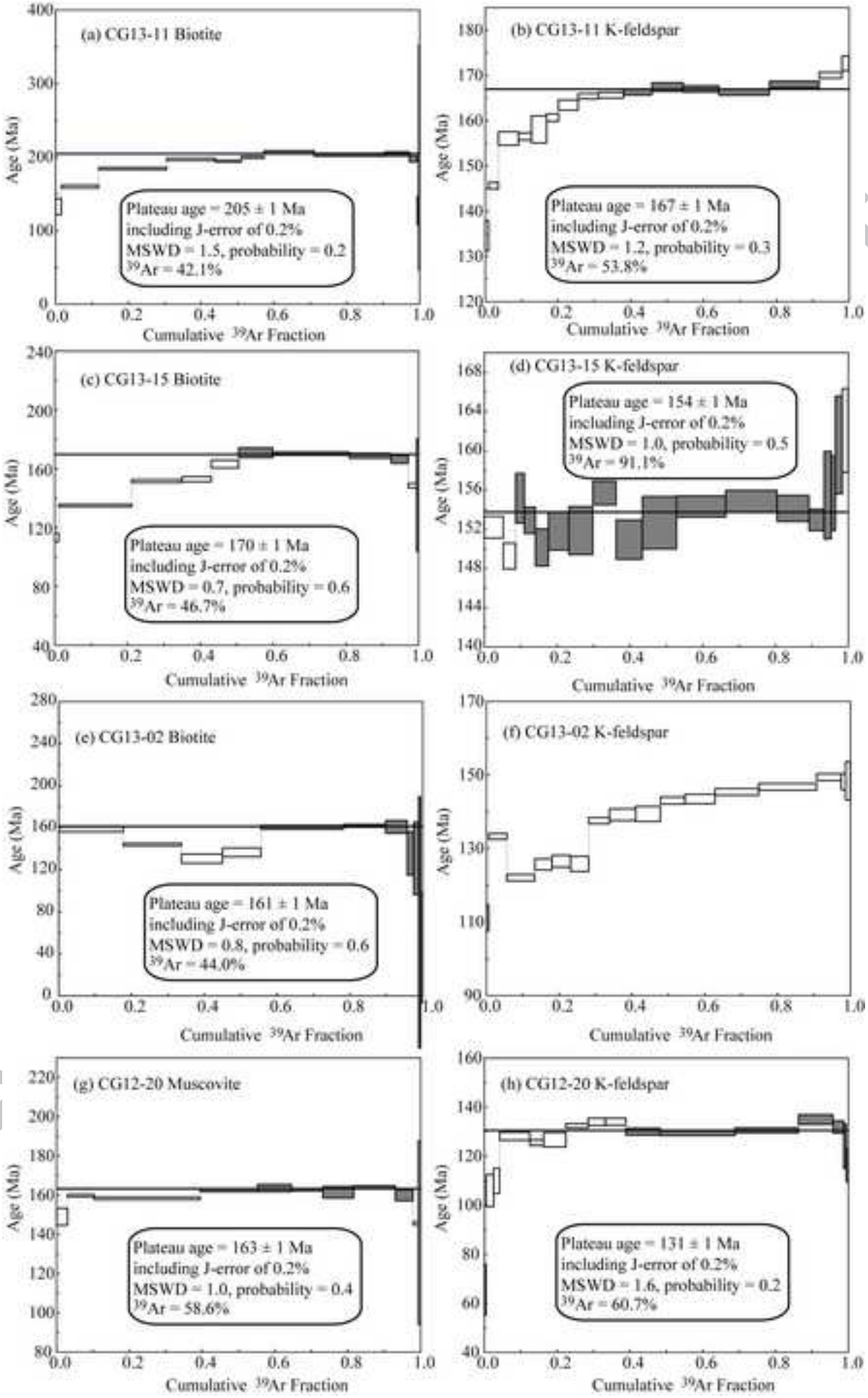

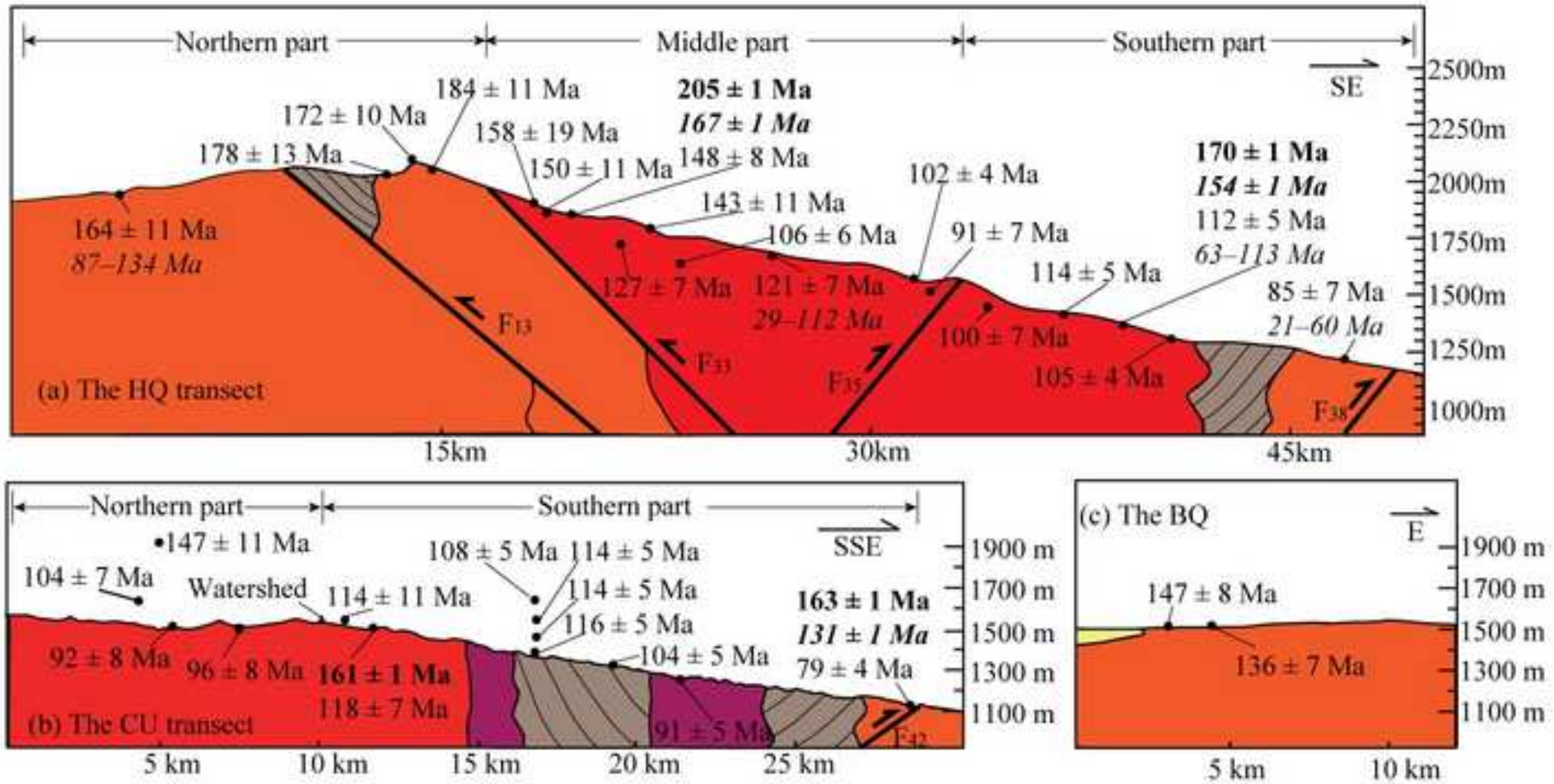

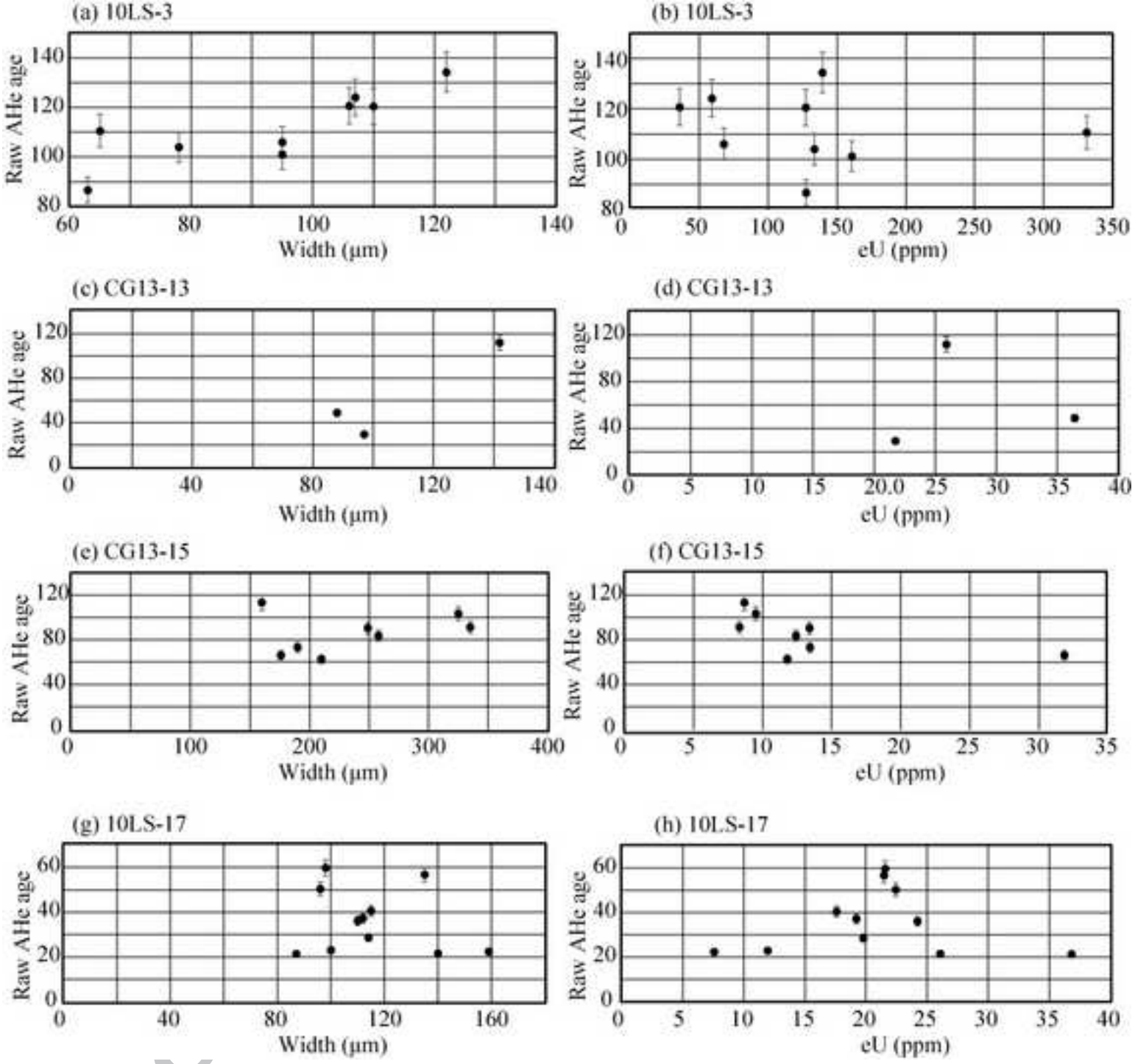

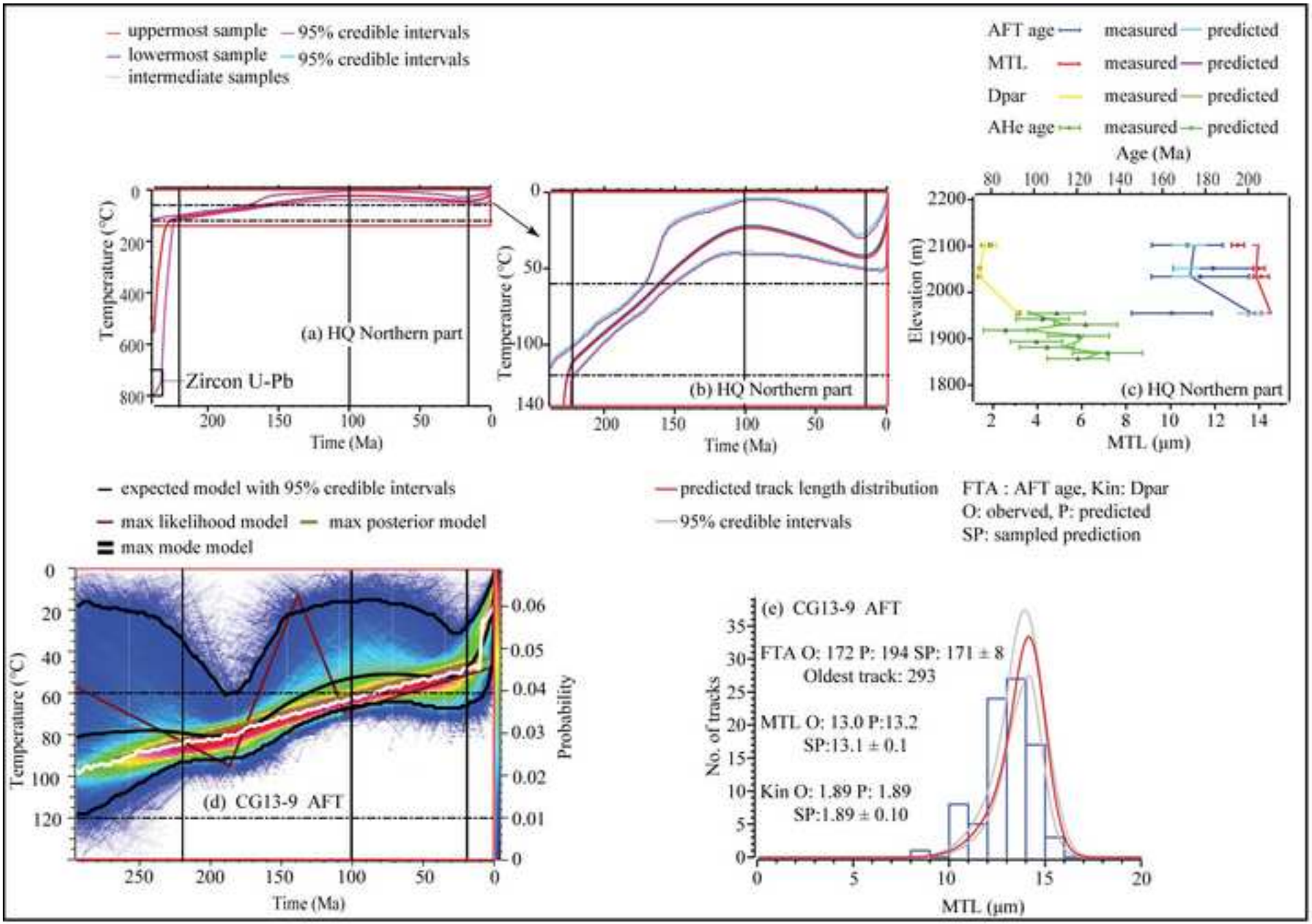

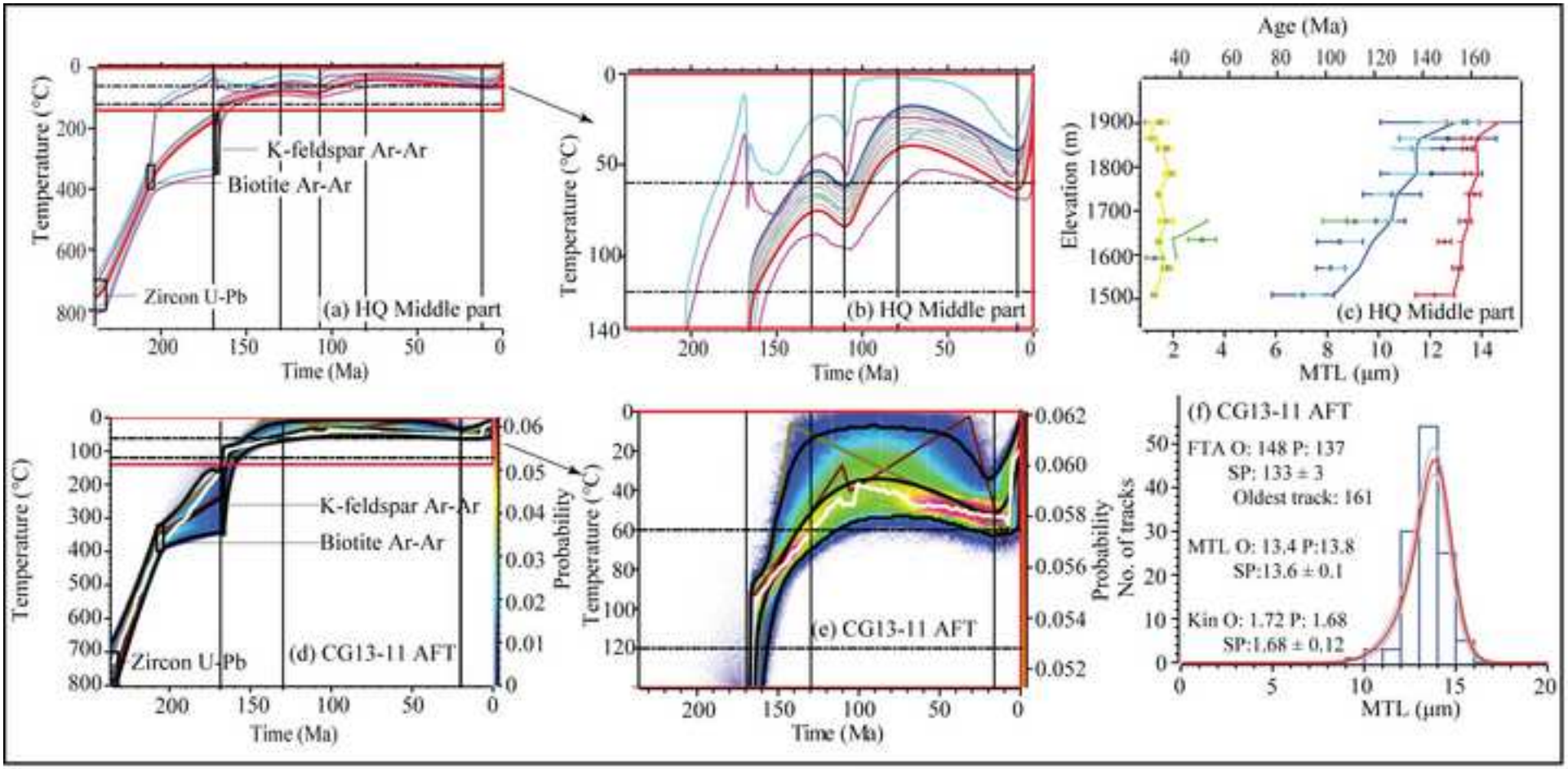

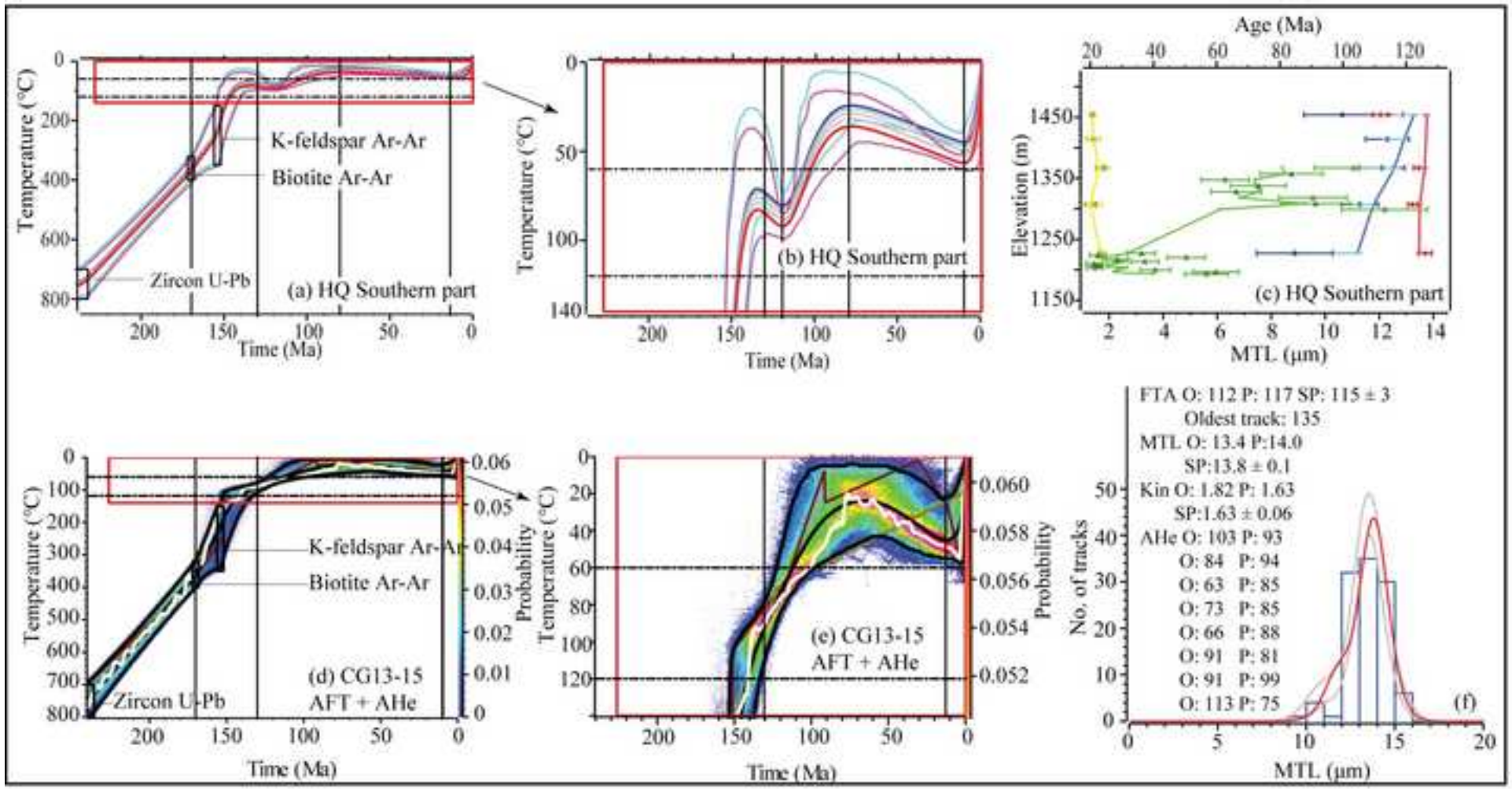

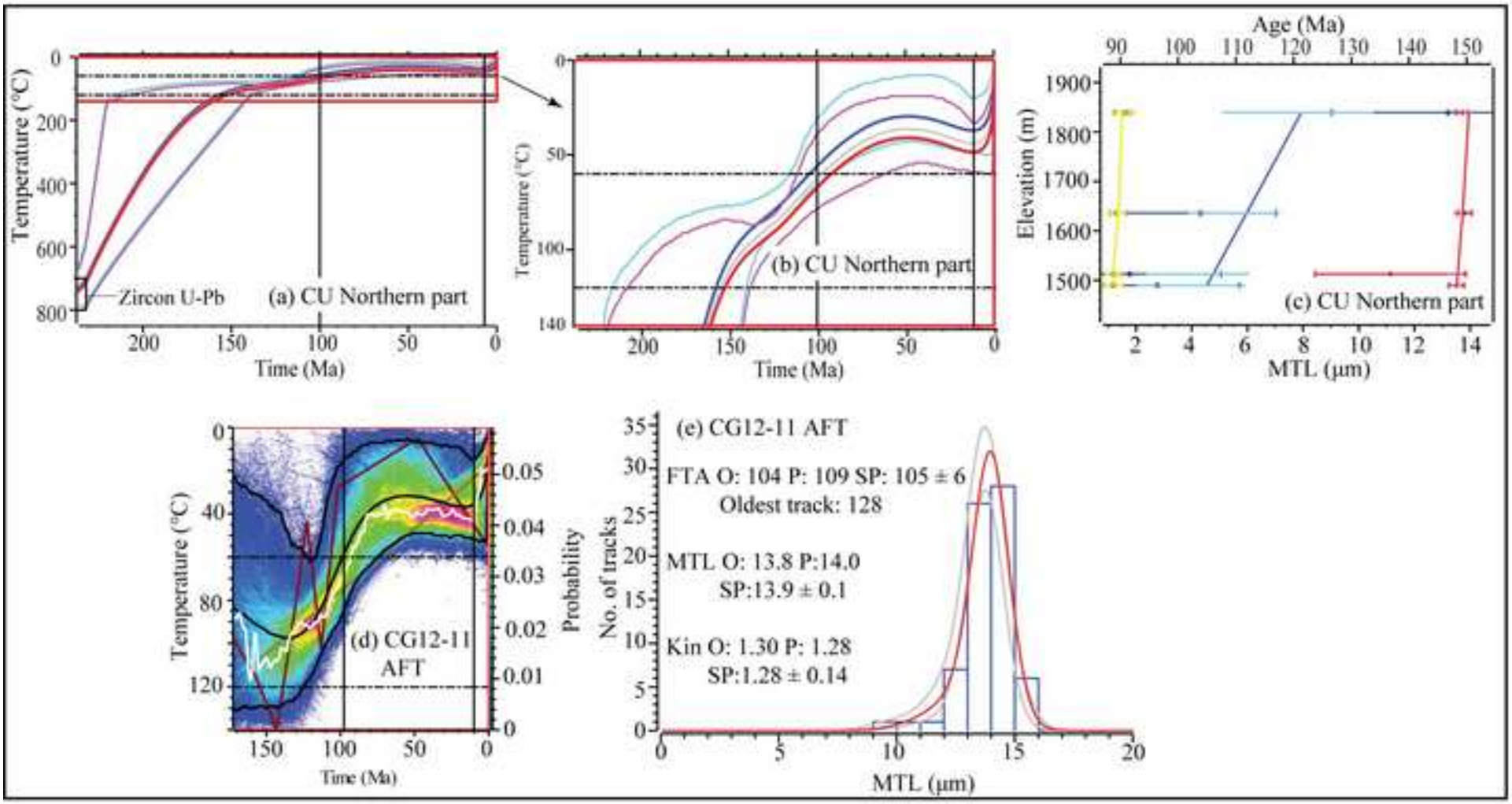

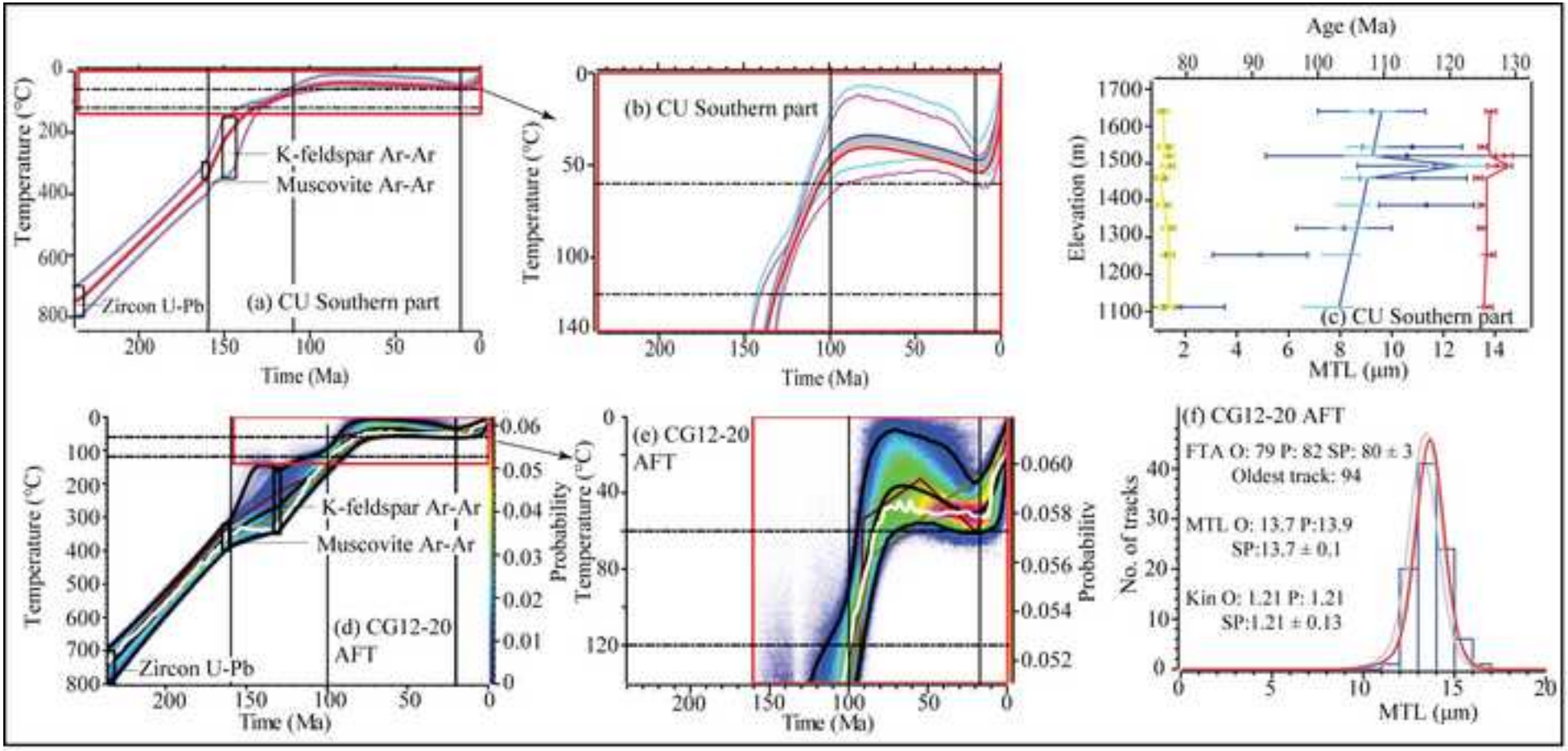

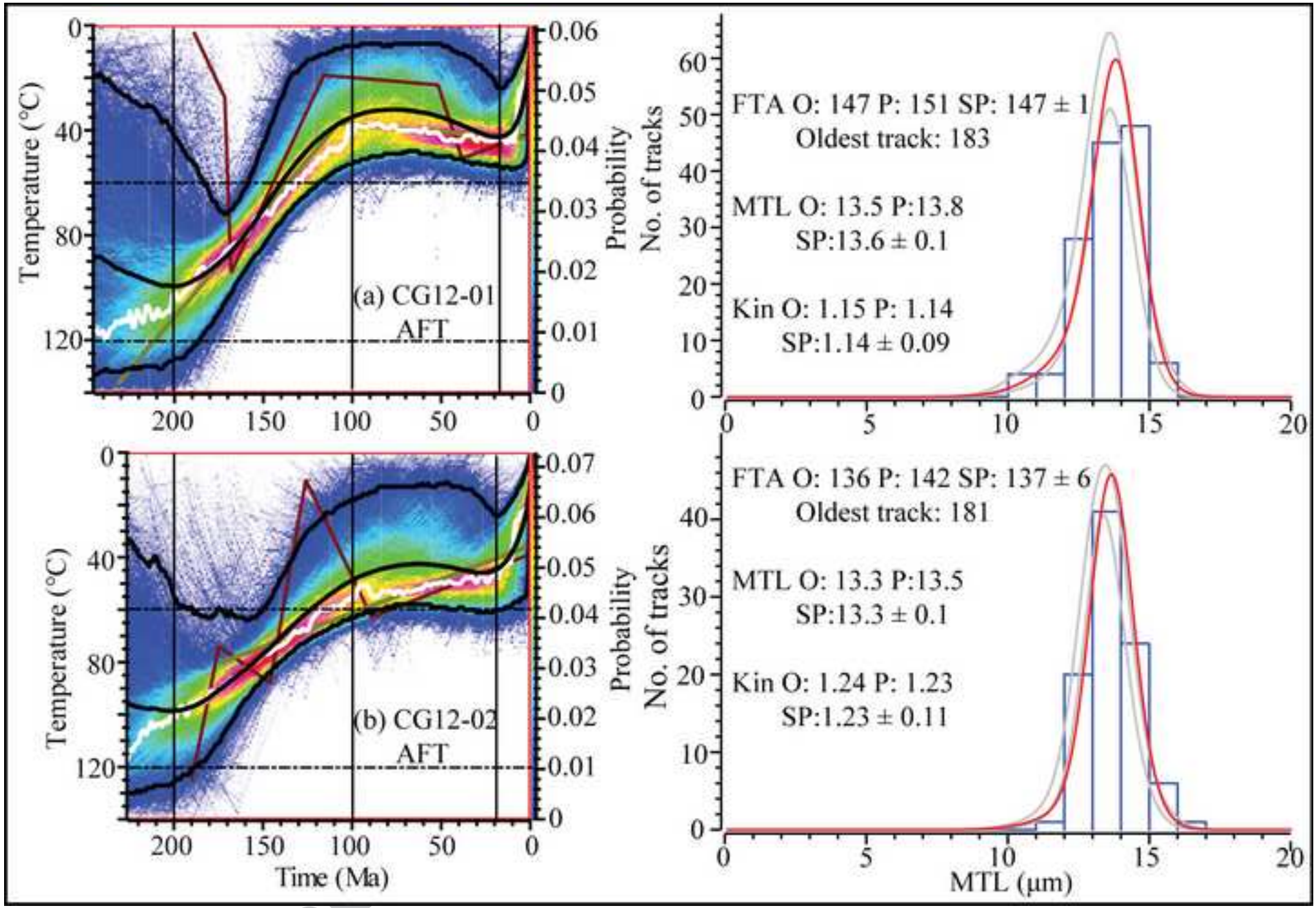

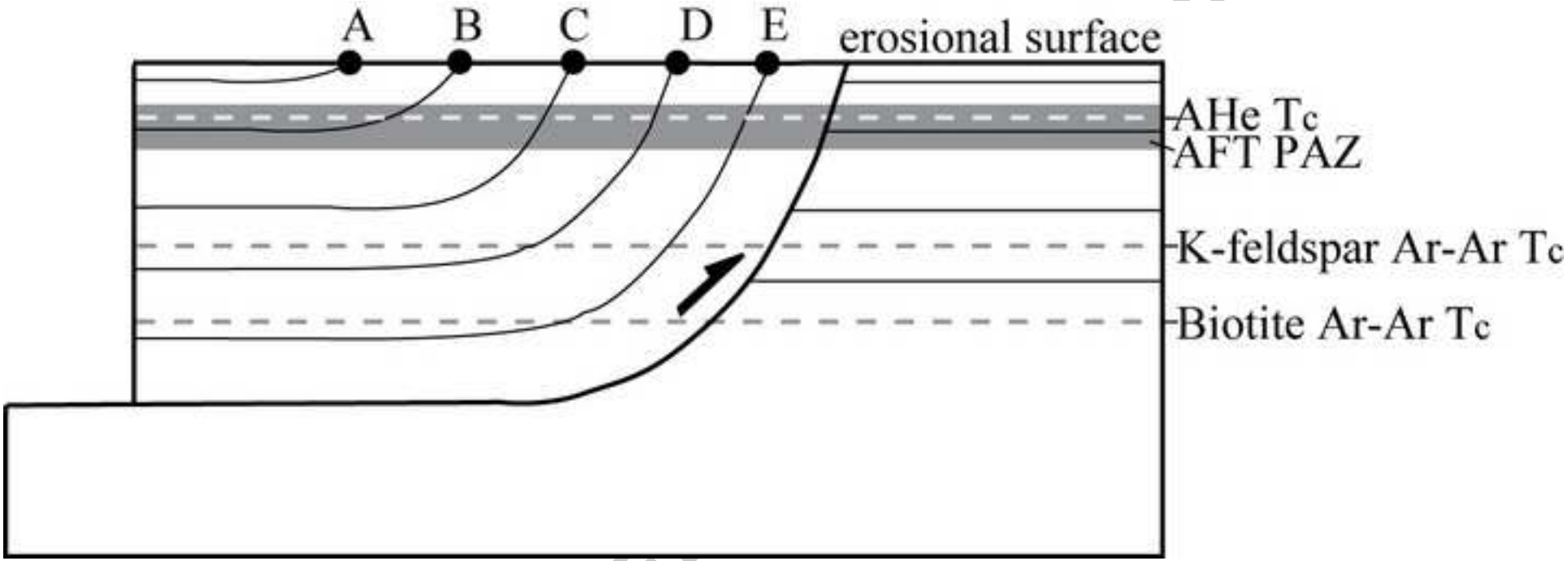

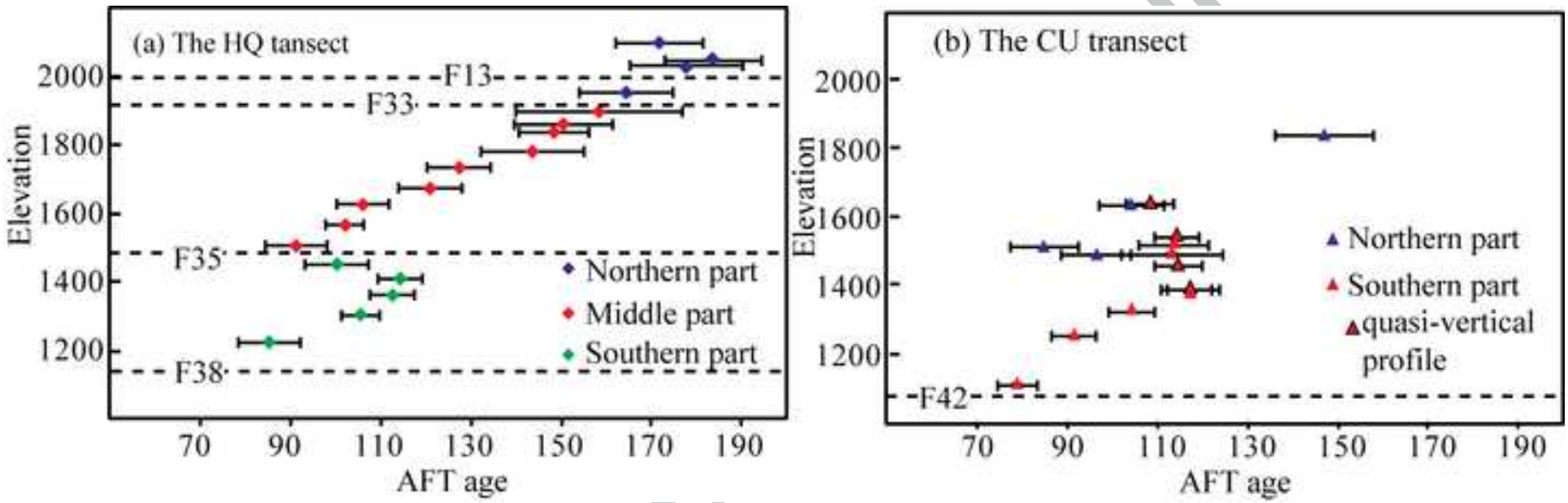

Table 2. Apatite fission track data in this study.

Table 3. Results of apatite (U-Th)/He analysis.

Table 4. Summary of the joint thermochronological data in this study.

Fig. SF1. Individual thermal history modelling in the HQ transect. See Fig. 7 for symbols.

Fig. SF2. Individual thermal history modelling in the HQ transect. See Fig. 7 for symbols.

Fig. SF3. Individual thermal history modelling in the CU transect. See Fig. 7 for symbols.

Fig. SF4. Individual thermal history modelling in the CU transect. See Fig. 7 for symbols.

Supplementary Table 1. Full summary of conventional $^{40}Ar/^{39}Ar$ data (uncertainties are reported at 2σ).

Supplementary Text 1. Multiple thermochronological analytical procedures.

Supplementary Text 2. Biotite/muscovite and K-feldspar $^{40}Ar/^{39}Ar$ ages.

Table 1

Sample details and methods used in this study.

Sample no.	Rock type	Pluton age (Ma)	Latitude	Longitude	Elevation (m)	Locality	Method
10LS-30	Granodiorite	270 ± 10	N41°12′52.7″	E106°38′31.0″	1955	The HQ transect	AFT, AHe
10LS-50	Granite	259 ± 5	N41°08′39.2″	E106°36′44.1″	2034	The HQ transect	AFT
CG13-09	Granite	259 ± 5	N41°08′17.9″	E106°36′48.1″	2102	The HQ transect	AFT
10LS-60	Granite	259 ± 5	N41°08′08.0″	E106°36′42.4″	2052	The HQ transect	AFT
CG13-10	Granite	236 ± 2	N41°06′32.1″	E106°36′25.1″	1902	The HQ transect	AFT
CG12-26	Granite	236 ± 2	N41°06′46.7″	E106°36′25.1″	1865	The HQ transect	AFT
C	Gr	236	N4	E1	18	The	B,

G13-1	anite	± 2	1°06′26.	06°37′1	42	HQ	K, AFT
1			5″	9.9″		transect	
			N4	E1		The	
1	Gr	236			17		
			1°06′15.	06°38′1		HQ	AFT
0LS-9	anite	± 2	7″	9.8″	38	transect	
C			N4	E1		The	
	Gr	236			17		
G13-1			1°06′10.	06°38′2		HQ	AFT
	anite	± 2			85		
2			9″	7.6″		transect	
1			N4	E1		The	
	Gr	236			16		
0LS-1			1°05′32.	06°38′3		HQ	AFT
	anite	± 2			30		
0			7″	5.7″		transect	
C			N4	E1		The	
	Gr	236			16		AFT
G13-1			1°04′38	06°38′5		HQ	
	anite	± 2			77		, AHe
3			″	0.6″		transect	
C			N4	E1		The	
	Gr	236			15		
G13-1			1°03′54.	06°42′6.		HQ	AFT
	anite	± 2			70		
4			5″	8″		transect	
1			N4	E1		The	
	Gr	240			15		
0LS-1			1°03′51.	06°42′0		HQ	AFT
	anite	± 2			09		
3			6″	9.8″		transect	
1			N4	E1		The	
	Gr	240			14		
0LS-1			1°03′31.	06°43′4		HQ	AFT
	anite	± 2			54		
4			6″	1.7″		transect	
1	Gr	240	N4	E1	14	The	AFT

0LS-15	anite	± 2	1°02′54.0″	06°44′36.0″	14	HQ transect	
CG13-15	Granite	240 ± 2	N4 1°02′27.8″	E1 06°45′11.1″	13 67	The HQ transect	B, K, AFT, AHe
0LS-16	Granite	240 ± 2	N4 1°01′48.3″	E1 06°45′29.3″	13 07	The HQ transect	AFT
0LS-17	Diorite	297 ± 2	N4 0°59′56.3″	E1 06°46′56.9″	12 27	The HQ transect	AFT, AHe
CG12-09	Granite	269 ± 2	N4 1°21′16″	E1 07°3′50.2″	18 39	The CU transect	AFT
CG12-11	Granite	269 ± 2	N4 1°21′31.8″	E1 07°3′45″	16 36	The CU transect	AFT
CG13-04	Granite	269 ± 2	N4 1°21′15.9″	E1 07°5′0.5″	15 13	The CU transect	AFT
CG12-14	Granite	269 ± 2	N4 1°20′17″	E1 07°5′13.7″	14 90	The CU transect	AFT
C	G	Prec	N4	E1	16	The	AFT

G12-2 1	neiss	ambrian	1°15′19.7″	07°3′14.2″	40	CU transect	
C G12-2 2	G neiss	Prec ambrian	N4 1°15′20.6″	E1 07°3′21.8″	15 44	The CU transect	AFT
C G12-2 8	Gr anite	241 ± 1	N4 1°18′30.3″	E1 07°4′38.9″	15 20	The CU transect	AFT
C G13-0 2	Gr anite	241 ± 1	N4 1°18′5.9″	E1 07°4′33.8″	14 93	The CU transect	B, K, AFT
C G12-2 3	G neiss	Prec ambrian	N4 1°15′22.4″	E1 07°3′31.7″	14 60	The CU transect	AFT
C G12-1 6	G neiss	Prec ambrian	N4 1°15′27.7″	E1 07°3′49″	13 87	The CU transect	AFT
C G12-1 7	G neiss	Prec ambrian	N4 1°14′25.5″	E1 07°5′5.7″	13 25	The CU transect	AFT
C G12-1 8	G neiss	Prec ambrian	N4 1°13′33.3″	E1 07°6′10.3″	12 53	The CU transect	AFT
C	Gr	260	N4	E1	11	The	M,

G12-20	anite	± 1	1°10′33.3″	07°8′34.7″	12	CU transect	K, AFT
CG12-01	Granite	262 ± 3	N41°46′31.7″	E107°20′38.9″	15 17	The BQ	AFT
CG12-02	Granite	262 ± 3	N41°46′39.5″	E107°21′44.1″	15 19	The BQ	AFT

Except for the pluton age of sample CG12-20, which is from Wu et al. (2013), the other pluton ages are our unpublished data. B = Biotite $^{40}Ar/^{39}Ar$ analysis, M = Muscovite $^{40}Ar/^{39}Ar$ analysis, K = K-feldspar $^{40}Ar/^{39}Ar$ analysis, AFT = Apatite fission track analysis, AHe = Apatite (U-Th)/He analysis.

Table 2

Fission track data in this study.

Sample no.	ρ_s (10^5/cm^2)	N_s	ρ_i (10^5/cm^2)	N_i	ρ_d (10^5/cm^2)	N_d	Age (Ma)	$P(\chi^2)$	MTL (μm)	N_{par}	SD (μm)
The HQ transect											
Northern part											
10LS-3	7.3	81	7.3	736	1.04	1494	164 ± 11	1.4	0.00	12.8 ± 1.8	4	1.2	3
10LS-5	3.6	69	4.2	49	1.04	1494	178 ± 13	1.4	0.99			1.4	1
CG13-09	1.04.0	39	1.08.4	52	1.01.2	1025	172 ± 10	1.0	0.91	11.6 ± 1.9	5	1.9	1
10LS-6	1 0.2	75	1 1.5	76	1 0.3	1494	184 ± 11	1.0	0.00	13.1 ± 1.4	8	1.3	1

Mi

ddle part

CG 13-10	5 .1	34	7 .4	93	1 1.3	64 5	1 58 ± 19	0	.8 2										1 .6	1
CG 12-26	6 .3	87	9 .9	05	1 1.7	64 5	1 50 ± 11	8	.9 9	1 2.4 ± 1.5							1 3		.3	1
CG 13-11	8 .3	63	1 2.6	46 6	1 1.2	02 5	1 48 ± 8	4	.9 9	1 2.3 ± 1.3							2 1		.7	1
10 LS-9	4 .6	66	5 .9	12 7	8 .2	73 6	1 27 ± 7	5	.9 2	1 2.7 ± 1.8							2 7		.5	1
CG 13-12	8 .8	12	1 3.8	92	1 1.2	02 5	1 43 ± 11	7	.8 8	1 2.3 ± 1.4							6		.9	1
10 LS-10	5 .5	10	8 .6	40 8	8 .1	73 6	1 06 ± 6	8	.9 9	1 1.1 ± 1.8							7		.5	1
CG 13-13	3 .9	51	7 .3	22 5	1 1.3	02 5	1 21 ± 7	0	.9 8	1 2.2 ± 1.8							4		.7	1
CG	8		1		1		1			1										1

13-14	.0	106	7.9	711	1.3	0225	02 ± 4	0	.90	1.7 ± 1.65	2	.8	
LS-13	10.3	360	3.1	5 56	8 .0	7336	9 1 ± 7	1	.99			.3	1
Southern part													
LS-14	10.7	595	5.7	902 0	7 .9	7336	1 00 ± 7	2	.00			.4	1
LS-15	10 0.6	334	1 3.9	1 079	7 .8	7336	1 14 ± 5	3	.96			.5	1
13-15	CG .4	659	6 3.0	1 371	1 1.3	0225	1 12 ± 5	0	.99	1 2.2 ± 1.5	0 9	.8	1
LS-16	10 2.1	031	1 7.8	1 464	7 .7	7336	1 05 ± 4	2	.00	1 1.8 ± 1.6	8 8	.6	1
LS-17	10.7	440	5 0.6	1 33	7 .6	7336	8 5 ± 7	1	.00	1 2.4 ± 1.4	2	.7	1

The

CU transect																
Northern part																
GG 12-09	3 .3	49	5 .5	84	1 2.2	80 7	47 ± 11	1 2	.9 9	2.6 ± 1.7	1 6	.6	1
CG 12-11	3 .4	59	4 .7	48	7 .3	63 8	04 ± 7	1 2	.0 0	2.7 ± 1.3	1 0	.4	1
CG 13-04	3 .5	92	8 .7	73	1 1.2	02 5	2 ± 8	9 1	.8 9			.2	1
CG 12-14	2 .9	35	4 .3	47	7 .7	63 8	6 ±8	9 7	.0 0	2.4 ± 1.2	1 9	.3	1
Southern part																
CG 12-21	4 .1	34 0	5 .7	88 3	7 .4	79 8	08 ± 5	1 5	.0 0	2.6 ± 1.3	1 3	.2	1
CG 12-22	1 0.3	99	1 3.6	63	7 .5	79	14 ±	1 3	.0	2.4 ±	1 4	.3	1

		2		6		8	5		0	1.2	2	
								1				
CG	2		4		7							1
						63	14 ±		.0			
12-28	.8	83	.2	28	.9			0				.4
						8	11		0			
								1				
CG	5		9		1							1
				51		02	18 ±		.0			
13-02	.1	20	.4		1.1			3				.4
				2		5	7		0			
								1		1		
CG	1		1		7							1
		66		22		63	14 ±		.9	2.2 ±	3	
12-23	0.5		4		.6			2				.2
		3		0		8	5		5	1.2	0	
								1		1		
CG	1		2		7							1
		31		09		63	17±		.0	2.3 ±	4	
12-16	8.2		4.3		.7			8				.3
		6		9		8	5		0	1.3	5	
								1		1		
CG	1		3		1							1
		47		30		80	04 ±		.0	2.1 ±	6	
12-17	7.9		8.5		1.8			0				.5
		0		9		7	5		0	1.3	5	
								9		1		
CG	1		1		7							1
		17		03		63	1 ±		.0	2.7 ±	2	
12-18	1.0		9.0		.8			6				.3
		4		0		8	5		0	1.3	5	
								7		1		
CG	1		2		7							1
				77		63	9 ±		.0	2.6 ±		
12-20	1.5	47	1.5		.3			2			3	.2
				9		8	4		0	1.3		
The BQ												
CG	1		1		1			1		1		1

12-01	0.4	79	8.4	37	2.9	80	47 ±	1	.9	2.4 ±	3	.2	
				7		7	8		4	1.4	5		
CG	1		2		1			1			1		1
				67		80	36 ±		.9	1.9 ±			
12-02	1.1	89	0.9		2.8			6			2	.2	
				7		7	7		5	1.5			

Note: ρ_s and ρ_i is spontaneous and induced fission track density, respectively; Ns and Ni is the number of spontaneous and induced fission tracks, respectively; ρ_d is interpolation of induced glass dosimeter CN5 track densities; Nd is the number of induced fission tracks in glass dosimeter CN5; T (± 1σ) is the AFT central age; n is the number of measured apatite grains in each sample; P (χ^2) is the probability of equaling; MTL (± 1σ) is the mean track length; N is the number of confined fission tracks in each sample; SD is the length standard deviation; Dpar is the mean etch pit figure diameter.

Table 3

Results of apatite (U-Th)/He analysis.

Sample	Grain #	^{4}He (cc)	^{238}U (ppm)	^{235}U (ppm)	^{232}Th (ppm)	(eU)[a]	[b]	Raw Age (Ma)	Corr Age (Ma)	Dispersion[e] (%)
10LS-3	1	1.9E-09	80.88	0.04	206.35	131.41	T	62	51	11	42
	2	2.7E-09	110.79	0.80	193.06	133.46	T	73	68	104	
	5	2.9E-09	46.03	0.33	54.13	59.08	T	68	07	124	
	6	1.7E-09	108.06	0.78	117.59	127.55	T	92	3	87	
	7	6.2E-09	30.14	0.22	32.19	35.57	T	27	06	121	
	8	5.6E-09	131.82	0.99	111.89	160.77	T	77	5	101	

		9	0	6	6	1					
	9	2.7E-09	55.44	.40	50.72	67.76	T	90	5	106	
	10	1.1E-08	116.18	.84	95.02	139.35	T	86	22	134	
	11	6.2E-09	104.86	.76	92.31	127.31	T	95	10	121	
	2	1.9E-09	21.82	.16	16.78	25.92	T	07	42	112	
CG13-13	4	3.4E-10	10.53	.08	109.84	36.42	T	47	8	49	130
	5	2.2E-10	14.90	.11	28.75	21.76	T	66	7	29	
CG13-15	1	5.5E-09	8.39	.06	4.54	9.51	T	00	25	103	58
	3	5.2E-0	11.23	.0	4.70	12.41	T	65	58	84	

		9		8							
	4	1.5E-09	9.11	.07	11.16	11.80	T	65	10	63	
	5	2.2E-09	11.36	.08	8.45	13.43	T	92	90	73	
	6	2.5E-09	11.43	.08	86.46	31.83	T	51	76	66	
	7	1.5E-09	11.25	.08	8.81	13.40	T	56	49	90	
	9	7.9E-09	7.33	.05	4.05	8.33	T	63	35	91	
	10	1.1E-09	6.96	.05	7.12	8.69	T	68	60	113	
10LS-1	1	4.3E-10	12.76	.09	48.35	24.21	T	92	10	36	10
7	2	1.0E-1	4.47	.0	13.04	7.57	T	35	59	22	8

	0		3						
	2								
		1		4	2				5
3	.6E-1		.0						
		2.81		0.56	2.43	T	54	6	0
	0		9						
	1								
		1		3	1				2
4	.5E-1		.0						
		1.29		5.79	9.78	T	12	14	9
	0		8						
	3								
		9		3	1				3
6	.4E-1		.0						
		.78		9.85	9.21	T	81	12	7
	0		7						
	1								
		2		6	3				2
7	.8E-1		.1						
		2.40		0.73	6.83	T	41	7	1
	0		6						
	1								
		6		2	1				2
8	.2E-1		.0						
		.06		4.91	1.96	T	00	00	3
	0		4						
	1								
		1		3	2				2
9	.7E-1		.1						
		6.70		9.41	6.08	T	40	40	2
	0		2						
	2								
1		1		2	1				4
	.8E-1		.0						
0		1.34		6.25	7.59	T	81	15	1
	0		8						
1	4	1		1	2				6
2	.6E-1	7.20	.1	8.06	1.57	T	74	8	0

0 2

8

1 1 4 2 5

.6E-1 .0

4 0.91 4.60 1.47 T 91 35 7

0 8

Note: a, eU (effective uranium) is calcultated as eUppm = [Uppm] + (0.235*[Thppm]); b, T = Number of terminations identified on crystal; c, L and W = Length and width of crystal or crystal fragment; d, UC = Estimate uncertainty, i.e., 6% standard deviation of repeat analysis of Durango apatite standards; e, dispersion = (maximum - minimum)/average, after Brown et al. (2013).

Table 4

Summary of the joint thermochronological data in this study.

Sample	Locality	Raw AHe Age		AFT		K-felds par $^{40}Ar/^{39}Ar$	Biotite/ Muscovite $^{40}Ar/^{39}Ar$
		rain #	Ma)	Closure temperature (°C)[a]	Central age (Ma)	AZ (°C)[b]	Closure temperature (°C)[c]	Closure temperature (°C)[d]
10LS-3	The HQ transect	1	11 ± 7	75	64 ± 5	0–120	11	20
		2	04 ± 6					
		3	24 ± 7					
		4	7 ± 5					

											21 ± 7
											01 ± 6
											06 ± 6
										0	34 ± 8
										1	21 ± 7
C G13-1 1	T he HQ transe ct	7 5	64 ± 11	1 0–1 20	67 ± 1	1 50–35 0	05 ± 1	2 20–40 0	3		
C G13-1 3	T he HQ transe ct	7 5	12 ± 7 9 ± 3	1 21 ± 7	0–1 20						

			9 ± 2								
			03 ± 6								
			4 ± 5								
			3 ± 4								
C G13-15	The HQ transect	3 ± 4	7 ± 5	12 ± 5	0–120	54 ± 1	50–350	70 ± 1	20–400	13	1
		6 ± 4									
		0 ± 5									
		1 ± 5									

		13		
	0	± 7		
		6 ± 2		
		2 ± 1		
		0 ± 3		
1	T he HQ transe ct	9 ± 2	5 ± 7	0–1 20
0LS-1 7		7 ± 2		
		1 ± 1		
		3 ± 1		

			2 ± 1						
		0	1 ± 2						
		2	0 ± 4						
		4	7 ± 3						
G13-0 2	T C he HQ transe ct			1 18 ± 7	0–1 20		1 50–35 0	61 ± 1	3 20–40 0
G12-2 0	T C he HQ transe ct			7 9 ± 4	0–1 20	31 ± 1	1 50–35 0	63 ± 1	3 00–35 0

Note: a, closure temperature for apatite (U-Th)/He analysis (°C) is from Wolf et al. (1996); b, apatite PAZ (°C) is from Gleadow et al. (1986); c, closure temperature (°C) for K-feldspar $^{40}Ar/^{39}Ar$ analysis is from Lovera et al. (1989); d, closure temperature (°C) for biotite $^{40}Ar/^{39}Ar$ is from McDougall and Harrison (1999); closure temperature

(°C) for muscovite $^{40}Ar/^{39}Ar$ is from Hames and Bowring (1994).

Highlights

- First constraint on the exhumation of the Langshan Mountains
- Biotite/muscovite and K-feldspar $^{40}Ar/^{39}Ar$, AFT, and AHe analyses
- Individual and joint thermal history modelling
- Impacts of thrusting on denudation

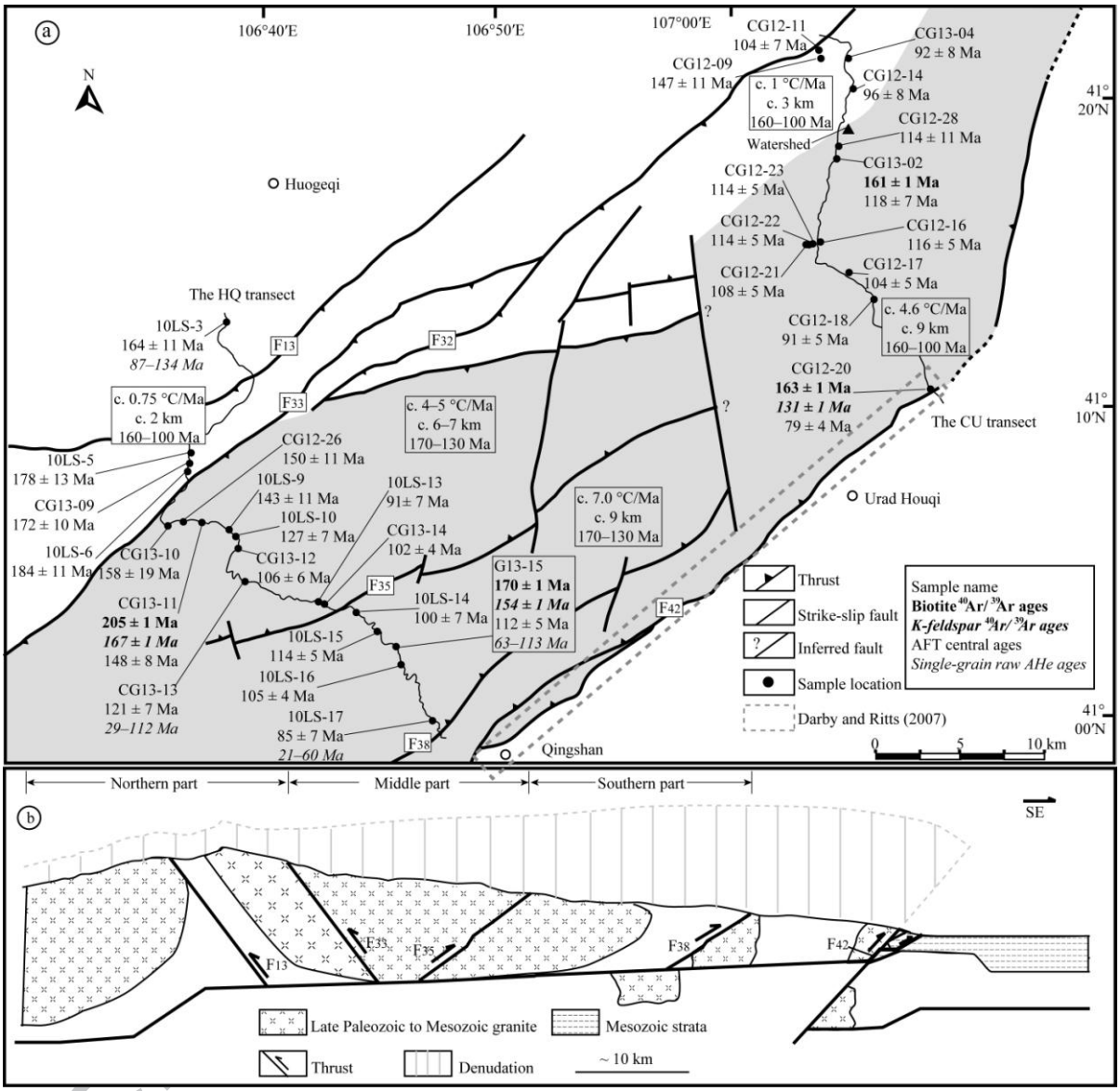

We the undersigned declare that this manuscript is original, has not been published before and is not currently being considered for publication elsewhere.

We confirm that the manuscript has been read and approved by all named authors and that there are no other persons who satisfied the criteria for authorship but are not listed. We further confirm that the order of authors listed in the manuscript has been approved by all of us.

We understand that the Corresponding Author is the sole contact for the Editorial process. He/she is responsible for communicating with the other authors about progress, submissions of revisions and final approval of proofs.

Signed by the corresponding author: